AGU PUBLICATIONS

JGR

Journal of Geophysical Research: Oceans

RESEARCH ARTICLE

10.1002/2017JC012982

The Lofoten Basin eddy: Three years of evolution as observed by Seagliders

Lu-Sha Yu[1,2,3], Anthony Bosse[2,4], Ilker Fer[2,4], Kjell A. Orvik[2], Erik M. Bruvik[2], Idar Hessevik[2], and Karsten Kvalsund[5]

[1]State Key Laboratory of Tropical Oceanography, South China Sea Institute of Oceanology, Chinese Academy of Sciences, Guangzhou, China, [2]Geophysical Institute, University of Bergen, Bergen, Norway, [3]University of Chinese Academy of Sciences, Beijing, China, [4]Bjerknes Centre for Climate Research, Bergen, Norway, [5]Runde Environmental Centre, Runde, Norway

Key Points:
- Lofoten Basin Eddy (LBE) core water properties show substantial interannual variability
- LBE is long-lived, with swirl velocity exceeding 0.7 m s^{-1} at 800 m depth and Rossby number close to unity
- Contrasting evolution of salt content in the core and surroundings implies a buffer zone near the eddy rim

Correspondence to:
I. Fer,
Ilker.Fer@uib.no

Citation:
Yu, L.-S., A. Bosse, I. Fer, K. A. Orvik, E. M. Bruvik, I. Hessevik, and K. Kvalsund (2017), The Lofoten Basin eddy: Three years of evolution as observed by Seagliders, *J. Geophys. Res. Oceans*, *122*, 6814–6834, doi:10.1002/2017JC012982.

Received 11 APR 2017
Accepted 25 JUL 2017
Accepted article online 31 JUL 2017
Published online 28 AUG 2017

Abstract The Lofoten Basin in the Norwegian Sea is an area where the warm Atlantic Water is subject to the greatest heat losses anywhere in the Nordic Seas. A long-lived, deep, anticyclonic eddy is located in the central part of the basin (the Lofoten Basin Eddy, LBE). Here we use observations from Seagliders, collected between July 2012 and July 2015, to describe LBE in unprecedented detail. The missions were designed to sample LBE repeatedly, allowing for multiple realizations of radial sections across the eddy. LBE has a mean radius of 18 ± 4 km and propagates cyclonically with a mean speed of approximately 3–4 cm s^{-1}. The anticyclonic azimuthal peak velocity varies between 0.5 and 0.7 m s^{-1}, located between 700 and 900 m depth. The average contribution of geostrophy in the cyclogeostrophic balance is 44%. The relative vorticity of the core is close to the local Coriolis parameter. The evolution of core water properties shows substantial interannual variability, influenced by surface buoyancy flux and advection of anomalous low-salinity near-surface waters that may affect the vertical extent of winter convection. A comparison of the eddy properties to those inferred from automated tracking of satellite altimeter observations shows that the location of eddy center is successfully detected to within one half eddy radius, but vorticity is underestimated and the radius overestimated, each approximately by a factor of 2, because of excessive smoothing relative to the small eddy radius.

1. Introduction

The inflow of warm and saline Atlantic Water (AW) into the Norwegian Sea with the Norwegian Atlantic Current (NwAC) can be considered as the northern limb of the meridional overturning circulation in the North Atlantic Ocean. The NwAC serves as a two-branch conduit of AW toward the Arctic Ocean and Barents Sea: an eastern branch as a nearly barotropic flow along the Norwegian continental slope and a western branch as a topographically steered jet along the Polar Front. Along its path, AW is continuously modified through heat and salinity loss before it subducts and returns to the North Atlantic as a western boundary current [*Poulain et al*., 1996; *Orvik and Niiler*, 2002].

Lofoten Basin (LB) in the Norwegian Sea acts as a reservoir for the northward flowing AW, with the two major branches of the NwAC on its eastern and western sides (Figure 1). Observations from Lagrangian drifters [*Poulain et al*., 1996; *Andersson et al*., 2011; *Koszalka et al*., 2011] and satellite altimetry [*Volkov et al*., 2013; *Raj et al*., 2015] show vigorous eddy activity in this area (see an example at 10°E, Figure 3). LB experiences intense heat loss to the atmosphere, losing more heat per unit area than any other region in the Nordic seas. The mean wintertime surface buoyancy flux is $-6\ (\pm 0.7) \times 10^{-8}$ m^2 s^{-3}, accounting for approximately 1/3 of the total buoyancy loss of the Nordic Seas, although it occupies only 1/5 of the total area [*Richards and Straneo*, 2015].

A prominent anticyclonic eddy in the center of LB was first discovered by the Russian oceanographic surveys in the 1970s and 1980s [*Alexeev et al*., 1991]. We call this anticyclonic eddy the Lofoten Basin Eddy (LBE). Since then, several studies addressed the mesoscale activity in the basin using observations of hydrography [*Ivanov and Korablev*, 1995b,1995a; *Rossby et al*., 2009a; *Raj et al*., 2015], numerical models [*Köhl*, 2007; *Volkov et al*., 2015], satellite altimetry [*Raj et al*., 2015, 2016; *Søiland et al*., 2016], and surface

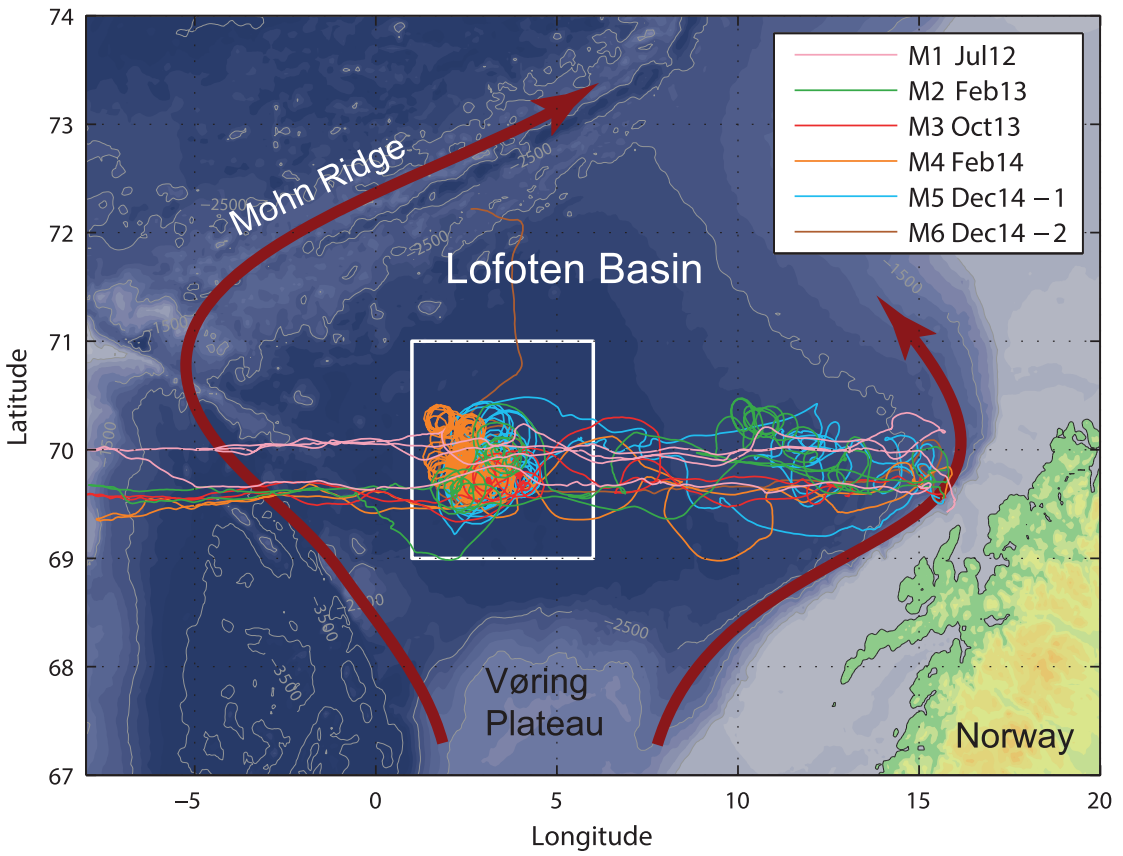

Figure 1. Map of the Lofoten Basin with the pathways of the Atlantic Water (dark red arrows), and tracks of the six Seaglider missions conducted between July 2012 and July 2015 (M1–M6). The white rectangle indicates the general area of LBE (1°E–6°E, 69°N–71°N) used for obtaining the background hydrography profiles.

drifters and subsurface floats [*Rossby et al*., 2009b; *Voet et al*., 2010; *Andersson et al*., 2011; *Koszalka et al*., 2013; *Søiland and Rossby*, 2013]. Lagrangian studies described the pathways, eddy kinetic energy, lateral mixing rates in the basin, as well as position and radius of LBE. Satellite altimeter studies exploited extensive sea level archives to quantify the regional statistics on cyclones and anticyclones, eddy-eddy interactions, and eddy advection, lifetime, and spatial distributions. Hydrographic and ocean current observations have been limited to cruises of opportunity and short duration surveys. The present consensus is that LBE is maintained by merging of anticyclonic eddies which drift westward after being shed off the eastern branch of the NwAC [*Köhl*, 2007; *Raj et al*., 2015; *Volkov et al*., 2015; *Raj et al*., 2016; *Søiland et al*., 2016]. The geometry of the basin attracts the anticyclones to the bottom depression and enables dynamical stability for the vortex. Winter convection plays an important role by providing a positive feedback, preconditioning for the subsequent winter and progressively deepening the core [*Ivanov and Korablev*, 1995b; *Köhl*, 2007]. LBE contributes to deep ventilation in the basin by promoting deep mixed layer and pooling of AW to depths exceeding 1000 m, thereby maintaining the substantial heat loss that occurs here. The understanding of the driving forces, seasonality, evolution, and maintenance of LBE is incomplete, and one plausible reason is a lack of robust winter observations.

A brief summary of the LBE characteristics emerging from the aforementioned studies is a stable anticyclonic vortex with a doubly convex lens structure, maximum swirl velocity at $O(10)$ km radius, and a 1000–1200 m deep central core in solid body rotation with a relative vorticity close to the negative Coriolis parameter. Direct observations based on trajectory of a RAFOS float captured in LBE for 9 months [*Søiland and Rossby*, 2013], show a cyclonic drift along the 3250 m contour, of approximately 4 cm s^{-1}. These observations agree well with earlier hydrographic surveys [*Ivanov and Korablev*, 1995b,1995a], satellite altimetry results [*Raj et al*., 2015], and eddy-resolving numerical simulations of *Volkov et al*. [2015], whereas *Köhl* [2007] suggests an anticyclonic drift.

Resolving the radial gradient in the eddy core that extends only to about 15 km from the center requires a high-resolution sampling strategy, which is rather difficult and expensive for classical shipboard measurements, especially during winter. Autonomous, relatively low-cost platforms such as ocean gliders can fill this gap [*Rudnick*, 2016]. Here we study LBE using Seaglider observations from six consecutive deployments from July 2012 to July 2015. The data set allows us to describe the evolution of the vertical and horizontal structure of LBE in time, and quantify its dynamical properties in detail, which was not possible before. Furthermore, we use the glider data set to evaluate the accuracy of satellite remote sensing measurements of the eddy parameters such as location, radius, relative vorticity, and kinetic energy.

2. Data and Methods

2.1. Seaglider Data and Methods

2.1.1. Seaglider Missions and Sampling

The hydrographic data were acquired using Seagliders during six missions covering from July 2012 to July 2015. The Seagliders [*Eriksen et al*., 2001] are autonomous, remotely piloted vehicles designed for multimonth missions, and sample the ocean along a sawtooth trajectory from sea surface to a maximum depth of 1000 m. They measure hydrographic parameters (e.g., temperature, conductivity, and pressure) while profiling vertically by changing their buoyancy and pitch angle. The vertical motion is translated into horizontal movement by wings. Depth-average currents (DAC) in the upper 1000 m are estimated from the difference between the Seaglider's dead reckoning and actual displacements as measured from surface GPS fixes.

A typical section in LB covers a distance of approximately 900 km from 16°E to 8°W along 69°40′N (Figure 1). Some missions covered the section back-and-forth twice, whereas others employed dedicated sampling within LBE and its surroundings. Duration of missions varied between 212 and 248 days (Table 1). These long-term missions required economic power consumption and a limited sampling rate, normally every 14–32 s. Typical glider vertical velocities varied between 7 and 10 cm s^{-1} during the missions, giving a vertical resolution of 1–3 m. All gliders were successfully deployed and recovered close to the shelf break.

The Seaglider offers a navigation mode well suited for piloting inside eddies whereby the glider steers relative to the DAC measured during the previous dive. By selecting this mode, the glider can be programmed to steer within $\pm 90°$ relative to the current set up by the eddy and thus moves into or out of the eddy in spiraling tracks. By using low angles, it is also possible to follow the current and dive at a relatively fixed distance from the eddy core. Spatial sampling was increased by using shorter and steeper dives within the LBE, with a dive time of about 4 h versus 9 outside. Gliders were first guided toward the approximate position of LBE, near 70degN, 3degE. Then, when caught by intense currents, the navigation mode enabled the gliders to spiral in and out of the eddy core, which could be identified as a warm deep layer with DAC values lower than 10 cm s^{-1}.

Details of the six missions (M1–M6) are listed in Table 1. The mission tracks are shown in Figure 1. The spiraling and circular tracks, especially in the central part of the basin (hereafter referred to as Eddy Sampling Tracks, ESTs) are generated by the navigation mode outlined above. All missions except M1 contain ESTs in the central LB. These ESTs are listed in Table 2, forming eight realizations (e1–e8) of the eddy, which will be analyzed for seasonal and annual variability of LBE.

Table 1. Details of the Six Seaglider Missions (M1–M6)

Seaglider	Mission	Period (Deployed/Recovered)	Duration (days)	Number of Dives	Number of Dives (<500 m)
sg559	M1	4 Jul 2012/25 Jan 2013	205	617	38
sg562	M2	14 Feb 2013/16 Sep 2013	214	680	5
sg561	M3	11 Oct 2013/17 Feb 2014	129	457	51
sg563	M4	26 Feb 2014/1 Nov 2014	248	831	4
sg562	M5	18 Dec 2014/19 Mar 2015	91[a]	340	3
sg559	M6	18 Dec 2014/18 Jul 2015	212	699	9

[a]M5 lasted 212 days, including sampling near the Mohn Ridge. Here the duration relevant to LB and LBE is listed.

The ct-sail (the part where the conductivity and temperature sensors are installed) of all gliders were either new or calibrated few months ahead of each mission. The ct-sail of sg562 was not calibrated between its two successive missions. Temperature and salinity measurements were compared to available hydrographic data managed by the Institute of Marine Research in Bergen, Norway (253 casts between July 2012 and 2016, within 69°N–71°N

Table 2. Details of Eddy Sampling Tracks (ESTs) for Eddy Realizations e1–e8

Eddy	Mission	EST Dives	EST Period	Duration (days)
e1	M2	89–129	12 Mar 2013 to 23 Mar 2013	11
e2	M2	319–370	29 May 2013 to 12 Jun 2013	14
e3	M3	122–157	18 Nov 2013 to 27 Nov 13	9
e4	M3	308–350	17 Jan 2014 to 27 Jan 2014	10
e5	M4	108–128	25 Mar 2014 to 31 Mar 2014	6
e6	M4	270–755	17 May 2014 to 6 Oct 2014	142
e7	M5	85–308	11 Jan 2015 to 10 Mar 2015	58
e8	M6	282–575	3 Mar 2015 to 11 Jun 2015	100

and 0°E–15°E). The glider temperature data are assumed to stay accurate to within 0.005°C according to the manufacturer calibration absolute accuracy (0.002°C) and drift (0.0002°C/month). Absolute Salinity was corrected by small offsets, constant for each mission, respectively, 0.0720, 0.0046, −0.0023, 0.0183, −0.0100, and 0.0022 g kg^{-1}. The offset values were obtained by a least squares fitting of the glider data between 700 and 1000 m to a reference linear *T/S* relationship corresponding to the mixing line between AW and the deep waters below 700 m. This method is similar to that previously used in *Bosse et al*. [2015, 2016] and provides a simple way to make large data sets carried out by different autonomous platforms consistent. The *T/S* relation was obtained from the available shipboard hydrographic data LB. The glider raw data were processed using the University of East Anglia Seaglider toolbox (http://bitbucket.org/bastienqueste/uea-seaglider-toolbox). The Conservative Temperature, Θ, and Absolute Salinity, S_A, were calculated using the thermodynamic equation of sea water [*IOC, SCOR, and IAPSO*, 2010].

2.1.2. Detection of Eddy Core and Generation of Radial Sections

Following the method used in *Bosse et al*. [2015], we determine the position of the LBE center, using profiles from ESTs. The method uses DAC and minimizes the cost function, $c(x,y)=\frac{1}{n}\sum_{i=1}^{n}\left(\mathbf{v_i}\cdot\frac{\mathbf{r_i}(x,y)}{\|\mathbf{r_i}(x,y)\|}\right)^2$, where $\mathbf{v_i}$ is the DAC velocity at the given position (x_i, y_i) and $\mathbf{r_i}(x,y)$ is the vector extending from (x, y) to (x_i, y_i). Here advection of the eddy center was not removed from DAC, because the advection is one order of magnitude smaller (about 5 cm s^{-1}) than the azimuthal eddy velocity exceeding 50 cm s^{-1}. The eddy center then corresponds to the location where DACs are the most perpendicular to the vectors joining their positions to the eddy center. Here we define the eddy radius as the radial distance from the core to where the orbital velocity reaches its maximum. We apply this method to moving sets of five consecutive velocity estimations, ensuring that the eddy drift over the minimization procedure is small (2–3 km) compared to its radius (15–20 km).

Once the LBE core is detected, the eddy is assumed symmetric, and the temperature, salinity, density profiles, and DACs are sorted according to their radial distance to the eddy center. LBE radial sections are then generated by gridding at 0.5 km radial bins and 1 m vertical bins, and smoothed over 10 km horizontally and 20 m vertically. The smoothing scales are chosen to remove the high-frequency and wavenumber variability associated with internal waves and other fine-scale processes, while retaining the dynamics associated with the *O*(10) km radius of LBE.

2.1.3. Dynamical Parameters and Cyclogeostrophic Velocity

The Rossby number can be written to represent the relative importance of the nonlinear terms in the momentum equation: $\mathrm{Ro}=U/Lf$ where f is the local Coriolis parameter and U and L are scales for azimuthal velocity and eddy size, respectively. The nonlinearity becomes important as Ro approaches unity, implying a violation of purely geostrophic balance. As will be shown below, LBE is highly nonlinear, and its momentum equation can be represented by a balance between the centrifugal, Coriolis, and pressure gradient forces. In cylindrical coordinates, the cyclogeostrophic balance can be written as

$$-\frac{v_c^2(r,z)}{r}-fv_c(r,z)=-\frac{1}{\rho_0}\frac{\partial p}{\partial r}=-fv_g(r,z), \tag{1}$$

where v_c is the cyclogeostrophic azimuthal velocity, r is the distance to the eddy center, z is depth, p is pressure, ρ_0 is density, and v_g is the geostrophic velocity field. The vertical component of the relative vorticity is $\zeta=\frac{\partial v_c}{\partial r}+\frac{v_c}{r}$.

For eddies characterized by relatively strong horizontal shear (greater than 0.1*f*), nonlinear terms (e.g., the centrifugal force) become important in the radial force balance. *Elliott and Sanford* [1986] showed that the peak azimuthal velocity in a subthermocline lens was underestimated when based on purely geostrophic balance.

From equation (1), we have solutions

$$v_c(r,z)=\frac{rf}{2}\times\left(-1\pm\sqrt{1+4\frac{v_g(r,z)}{rf}}\right). \quad (2)$$

The negative root of equation (2) is centrifugally unstable [*McWilliams*, 2006], and we use the positive root to compute the cyclogeostrophic velocities [see also *Pelland et al*., 2013]. To estimate the cyclogeostrophic velocities from the glider data, we follow the method outlined in *Bosse et al*. [2016]. Decomposing the velocities v_c and v_g into depth-averaged ($\overline{v_c}$ and $\overline{v_g}$) and baroclinic (v_c' and v_g') components, and then vertically averaging equation (2) results in terms including the depth-averaged velocities and the geostrophic shear, $v_g'(r,z)$. $\overline{v_c}$ can be approximated by the DAC measured by the glider. $v_g'(r,z)$ is obtained by vertically integrating the thermal wind balance from the radial density sections generated as described in section 2.1.2. The unknown geostrophic component of DAC, $\overline{v_g}(r)$, can be solved for from the vertically averaged form of equation (2). This geostrophic depth-average velocity is then used to infer absolute geostrophic velocities $v_g(r,z)=\overline{v_g}(r)+v_g'(r,z)$. Finally, cyclogeostrophic velocities are computed from equation (2).

2.1.4. Mixed-Layer Depth and Columnar Buoyancy

The mixed-layer depth (MLD) is calculated following *de Boyer Montégut et al*. [2004], as the depth where the potential density anomaly, σ_θ, first exceeds the near surface value (upper 10 m average) by 0.03 kg m^{-3}. LBE has a weakly stratified core, which can easily be mixed by convection. During winter, the LB loses buoyancy, resulting in convective mixing of the initially stratified water column down to some depth. To quantify the preconditioning of the water column to vertical mixing, we compute the columnar buoyancy, $IS(z)=\int_0^z N^2(Z)ZdZ$ [*Bosse et al*., 2015] where $N^2(z)=-\frac{g}{\rho_0}\frac{\partial\sigma_\theta}{\partial z}$ is the buoyancy frequency squared, computed from the smoothed density over 20 m vertical scale. When the lateral advection of buoyancy is negligible, *IS* corresponds to the time-integrated buoyancy loss required for mixing the water column down to *z*. Therefore, for a uniform buoyancy loss across LBE, a smaller *IS* indicates the potential for deeper convective mixing.

2.1.5. Heat and Salt Content Anomaly

The heat and salt content anomaly of LBE are evaluated with reference to a background field. Background temperature and salinity, $\overline{\Theta}$ and $\overline{S_A}$, are constructed by averaging all profiles collected outside the eddy, but within an area encompassing the LBE drift, and within $\pm$15 days around each ESTs (see Figure 1 for the extent of background field). The anomalies of Conservative Temperature and Absolute Salinity are computed along isopycnal layers from the gridded fields for each eddy realization. The heat content anomaly per volume is $\rho C_P\left(\Theta-\overline{\Theta}\right)_\sigma$, and similarly, the salt content anomaly per eddy volume is $\rho\left(S_A-\overline{S_A}\right)_\sigma$, where the operator $(\cdot)_\sigma$ indicates difference along an isopycnal layer. The volume integration for heat and salt content is then performed from surface to 1000 m vertically, around a full circle (0–2π), and in two distinct radial ranges exhibiting different water mass properties: the core region, including the velocity maximum ($0<r<20$ km) and the rim of the eddy ($20<r<40$ km).

LBE has a deep core extending approximately 200 m further below the maximum depth of the glider sampling. The core is typically warmer and saltier than the background field for this deep isopycnal, hence the heat and salt content anomaly of the LBE core are underestimated.

2.2. Eddy Detection From Satellite Altimeter Data

We use the "all-sat-merged" absolute dynamic topography (ADT) satellite altimeter product from January 2012 to September 2015 to independently quantify the LBE sampled by Seagliders. The merged products are available every 7 days in a 1/4° × 1/4° grid. ADT contains the contents of gridded sea surface heights above geoid, and is the sum of sea level anomaly (SLA) and mean dynamic topography. Following the automated algorithm described by *Halo* [2012], we detect LBE according to two criteria: closed contours of sea surface height (SSH) [*Chelton et al*., 2011], and a negative Okubo-Weiss parameter, *W* [*Isern-Fontanet et al*., 2006; *Chelton et al*., 2007]. *Halo* [2012] showed that the two-criteria method is more robust than using any one of them separately. The Okubo-Weiss parameter is defined as $W=S_h{}^2+S_t{}^2-\omega^2$, with

$$S_h=\frac{\partial V_g}{\partial x}+\frac{\partial U_g}{\partial y},$$

$$S_t=\frac{\partial U_g}{\partial x}-\frac{\partial V_g}{\partial y},$$

$$\omega = \frac{\partial V_g}{\partial x} - \frac{\partial U_g}{\partial y},$$

where U_g and V_g are the surface geostrophic velocities deduced from ADT. S_h is the shearing deformation rate, S_t the stretching deformation rate, and ω the relative vorticity of the geostrophic current. Note the different notation used here for the surface velocity and vorticity. These variables are based on the geostrophic balance only, unlike the glider measurements, which take into account the cyclogeostrophic balance.

Halo et al. [2014] conclude that the use of SSH data rather than sea level anomaly (SLA) data has two advantages. Spurious detection of current meanders, which are often related to the closed sea level anomaly loops, are excluded, and erroneous interpretation of negative SLA as cyclonic eddies in a system dominated by large anticyclonic eddies is avoided.

Eddies in the LB are identified in three steps. First, we calculate W based on the geostrophic velocity, use two passes of a Hanning filter to reduce the grid-scale noise, and then select regions dominated by vorticity ($W < 0$). Second, regions inside a closed loop of SSH are selected by choosing the interval between successive contours of 2 cm, consistent with the altimetry precision in this region [*Volkov and Pujol*, 2012]. A diameter limit of 500 km is set to prevent selecting a basin-scale gyre as a closed loop. Third, we select the regions of negative W embedded in closed SSH contours. We obtain a more consistent pattern than the spurious detection associated with noisy W signal, and the ambiguities in multipoles/elongated closed loops are excluded. More details about the method can be found in *Halo* [2012] and *Halo et al*. [2014]. In this study, we only concentrate on LBE, and choose this eddy manually from the resulting set of eddies.

The radius of LBE from the altimeter data is calculated from the respective surface area (A), as $R_{\mathrm{sat}} = \sqrt{A/\pi}$. As noted by *Isern-Fontanet et al*. [2006], the closed lines with $W = 0$ (the eddy edge) is approximately equivalent to the location of maximum orbital velocities, consistent with our definition for the Seaglider data.

2.3. Surface Buoyancy Flux

The surface buoyancy flux, B_0, affects the distribution of density in the near-surface waters and is the dominant driver of winter variations in MLD in the Lofoten Basin [*Nilsen and Falck*, 2006]. A destabilizing buoyancy flux ($B_0 < 0$) leads to convection whereas a stabilizing buoyancy flux strengthens the surface stratification. The surface buoyancy flux B_0 which depends on the heat and freshwater fluxes can be written as [*Richards and Straneo*, 2015]

$$B_0 = \frac{g\alpha}{\rho_0 C_p}(Q_s + Q_l + Q_R) + \frac{g\beta\ \mathrm{SSS}}{\rho_0}(P - E), \tag{3}$$

where $g = 9.8$ m s^{-2} is the acceleration due to gravity, α and β are the thermal expansion and haline contraction coefficients for seawater, $\rho_0 = 1027$ kg m^{-3} is the reference density, C_p is the specific heat for seawater, and SSS is the sea surface salinity (measured in practical salinity scale). The terms Q_s, Q_l, and Q_R are the sensible, latent, and net radiative heat fluxes (Q_R is the sum of the surface net longwave radiation Q_{lw} and the surface net shortwave radiation Q_{sw}), and P and E are the precipitation and evaporation, respectively. Radiation terms, heat fluxes terms, P, and E are obtained from ERA Interim [*Dee et al*., 2011]. SSS is obtained from the 1/12° resolution operational Mercator global ocean analysis and forecast system (Copernicus, Marine Environment monitoring service, product GLOBAL_ANALYSIS_FORECAST_PHY_001_024). B_0 is calculated at the grid point (70°N, 3°E), representative of the typical position of LBE.

3. Environmental Conditions During Missions

3.1. Atmospheric Forcing

Atmospheric forcing (2 weekly moving averaged values) during the measurement period is shown in Figures 2a and 2b. At the location (70°N, 3°E), the largest wind speeds (from ERA Interim) occur in late January to early March every year, with the 2 week averaged speeds of 10 m s^{-1} (instantaneous values exceed 20 m s^{-1}). The LB loses buoyancy during almost 8 months from late August to late April every year. The buoyancy

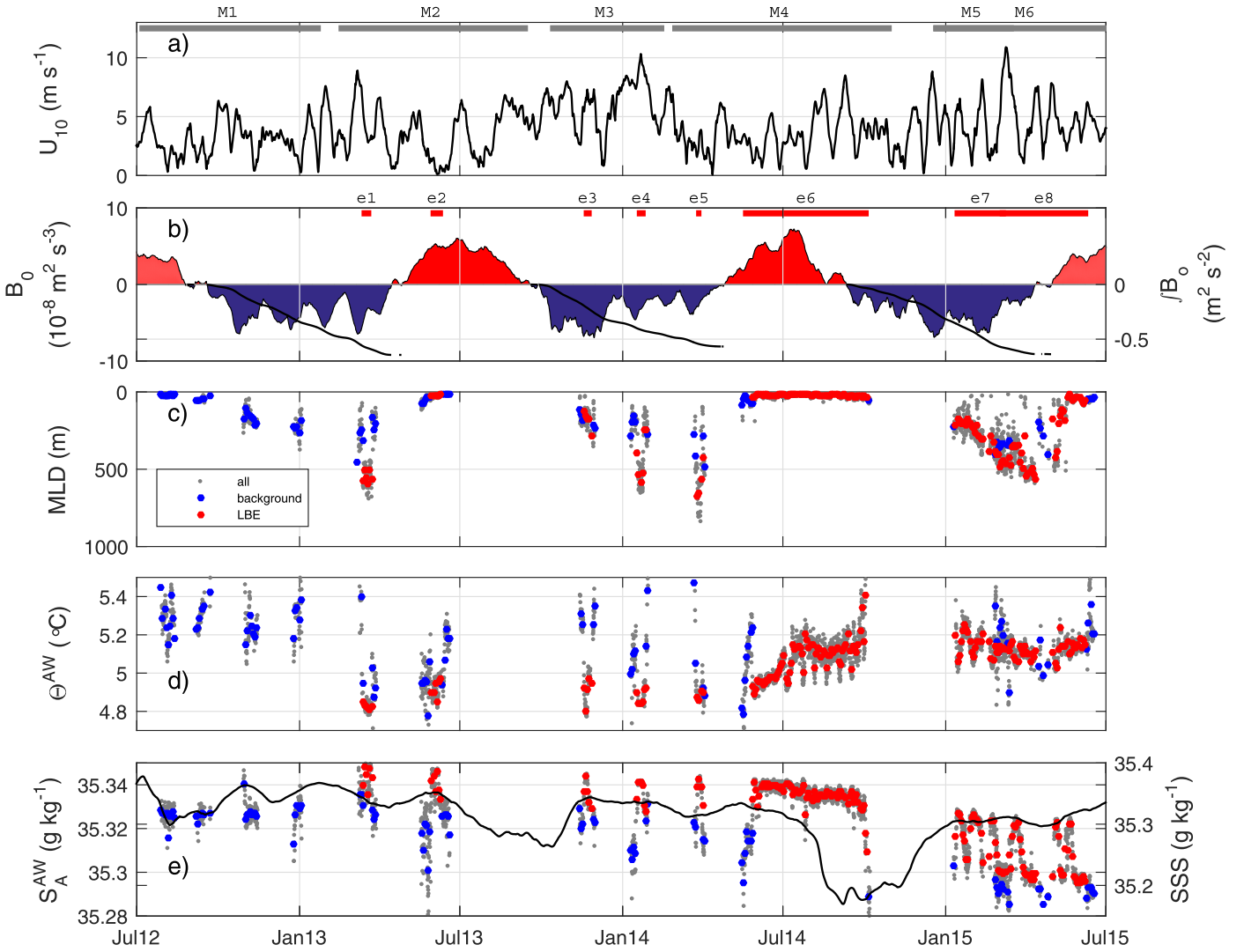

Figure 2. Time series of (a) 10 m wind speed, U_{10}, (b) surface buoyancy flux, B_0, and (right axis) time-integrated buoyancy loss for each winter period, (c) mixed-layer depth, MLD, (d) mean Conservative Temperature and (e) Absolute Salinity of the Atlantic Water ($\sigma_\theta < 27.9$ kg m^{-3}), and 2 weekly moving averaged SSS from global reanalysis (here converted to Absolute Salinity, black line, right axis). Surface forcing is derived from ERA Interim at (0°E, 70°N), and presented as 14 day moving averages. In Figures 2c–2e, data are bin-averaged over 2 days and profiles carried out within LBE are plotted in red, in the LBE region but outside the eddy in blue (see Figure 1 for the definition of the eddy area), and outside the LBE region in gray. Time coverage of glider missions (M1–M6) are marked in Figure 2a). Eight eddy realizations sampled during ESTs are marked by e1–e8 in Figure 2b).

flux averaged over the 8 month-long periods of buoyancy loss each year from 2012 to 2014 is -3.2×10^{-8} m^2 s^{-3}, and varies to within 10% interannually. The 2012–2013 and 2014–2015 winters, however, lose more buoyancy than in 2013–2014, with the cumulative buoyancy loss of 0.64 m^2 s^{-2} (in 2012 and 2014), compared to 0.57 m^2 s^{-2} in 2013. For comparison, *Richards and Straneo* [2015] reported December–January–February average buoyancy flux of $-6.0\ (\pm 0.7) \times 10^{-8}$ m^2 s^{-3} in LB, and $-3.8\ (\pm 0.5) \times 10^{-8}$ m^2 s^{-3} in the entire Nordic Seas, using ERA Interim data between 1979 and 2012. In this location, precipitation typically exceeds evaporation. The averaged heat flux contribution (the first term in equation (3)) is 3 times greater than the averaged freshwater contribution (the second term) in winter time (here defined as periods of negative surface buoyancy flux), and 4 times larger in summer time, indicating that the surface heat fluxes are dominating terms in B_0.

3.2. Mixed-Layer Depth

The MLD values during times when Seagliders sampled in LBE realizations e1–e8 are marked with red dots in Figure 2c, whereas the background values in the general LBE region (but outside the eddy), bounded by 69°N–71°N and 1°E–6°E (see Figure 1) are shown in blue. Both inside and around LBE, the MLD shows

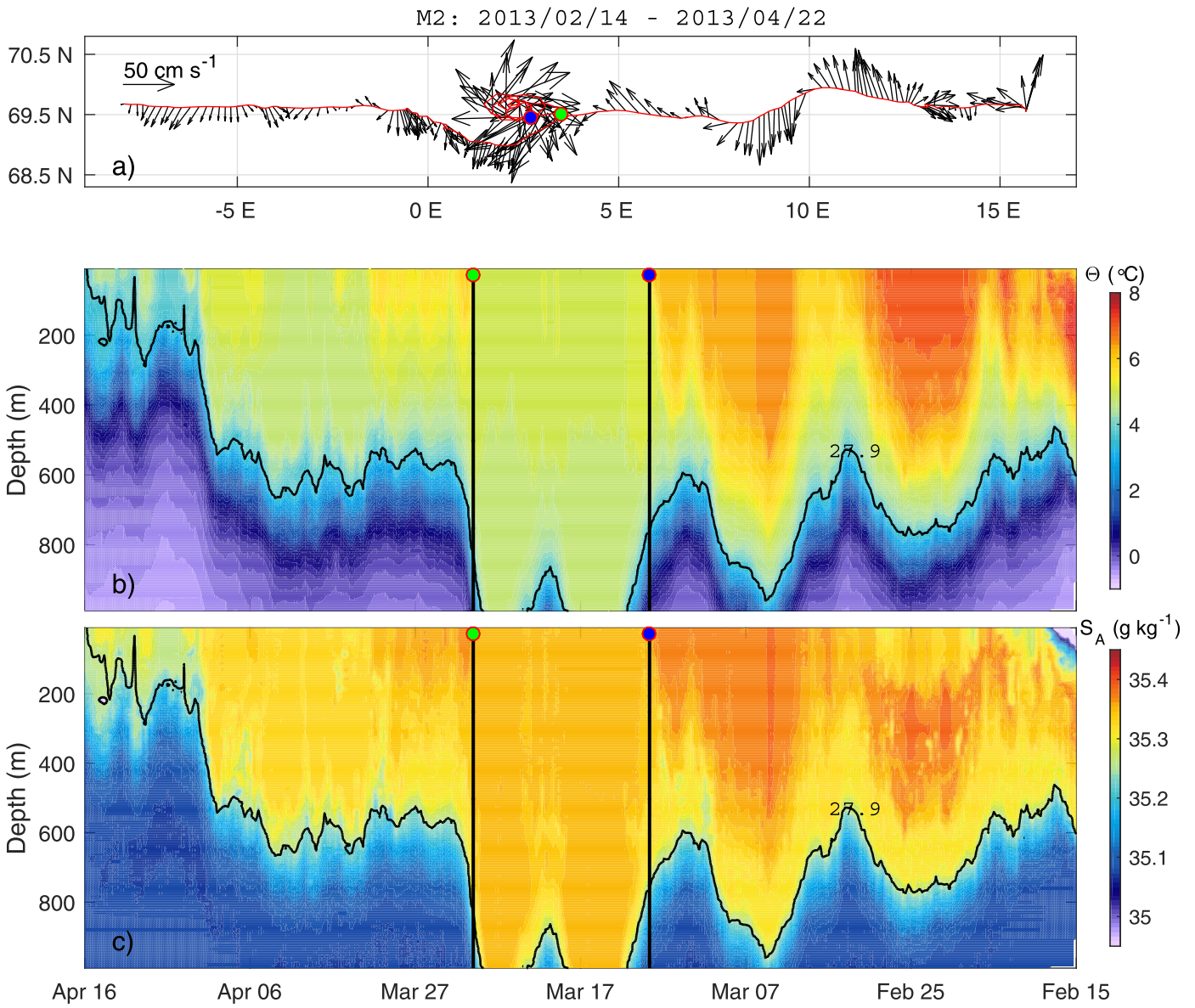

Figure 3. Zonal temperature and salinity section from the M2 mission (15 February to 16 April 2013) crossing LBE (between the blue and green circles). (a) The glider track together with the 1000 m depth-averaged currents (DAC). (b) Conservative Temperature and (c) Absolute Salinity section along the track from surface to 1000 m, with the 27.9 isopycnal contour in black delimiting the lower part of the Atlantic Water layer. Times of entrance and exit of LBE are indicated by vertical lines and corresponding blue and green circles. Note the time axis is reversed to roughly correspond with the mission direction from east to west.

seasonal and interannual variability caused by surface buoyancy forcing and preconditioning of the water column. The MLD starts to deepen by mid-October each year and reaches its maximum depth between mid-March in 2013 and mid-April in 2015. MLD is deeper inside LBE relative to the background (see red and blue dots in Figure 2c). The deepest MLD is observed by the end of March 2014 (798 $\pm$ 19 m, mean and one standard deviation observed within 1 week centered around the MLD maximum). This period is followed by restratification and stabilizing surface buoyancy forcing, until October, when the MLD is the shallowest, typically 10–60 m deep. Winter 2014 is the most intense in terms of vertical mixing, compared to MLD of 667 $\pm$ 17 m in 2013, and 570 $\pm$ 10 m in 2015. However, the cumulative buoyancy loss is 10% smaller than during the other winters (Figure 2b). This can be attributed to uncertainties in the surface forcing, but also stress the importance of oceanic preconditioning to deep mixing by the mesoscale. This is well illustrated by the shallower MLD maxima observed outside LBE (319 $\pm$ 95 m, 453 $\pm$ 52 m, and 348 $\pm$ 27 m from 2013 to 2015) in a region experiencing similar atmospheric forcing.

3.3. Atlantic Water Evolution From 2012 to 2015

Thanks to an intense effort in deploying gliders, water mass properties could be sampled almost continuously for 3 years. AW is usually defined as temperatures above 3°C and salinity above 35 in the practical salinity scale (corresponding to about 35.2 g kg^{-1} in S_A). Here we define AW as waters lighter than 27.9 kg m^{-3}, which is slightly more restrictive than the Θ-S_A thresholds (see sections shown in Figure 3). Figures 2d and 2e shows the interesting evolution of AW properties over the study period. Apart from temperature fluctuations that can be explained by winter cooling, there is a general trend toward fresher AW: salinity dropped from 35.34 $\pm$ 0.01 to 35.29 $\pm$ 0.01 g kg^{-1}, from summer 2012 to summer 2015. The average and one standard deviation are calculated over the first half of June each year, a common period when data were collected each year. Inside LBE (red markers), the evolution is quite different, especially for temperature which increased from 4.97 $\pm$ 0.11 to 5.23 $\pm$ 0.12°C, reaching values observed in the basin. However, AW salinity observed within LBE stayed always about 0.02 $\pm$ 0.01 g kg^{-1} above the background values and followed the exterior freshening. The drop in salinity does not follow a gentle trend, but occurs mostly between spring and summer 2014. SSS from the global reanalysis (see the black line in Figure 2e) shows a freshening each summer in the center of the basin, consistent in terms of amplitude and timing with the freshening observed with the gliders. In the model, fresh waters appear along the Norwegian coast in spring and further migrate toward the basin in summer, typically by the lateral advection by mesoscale eddies (observed in the time-lapse fields of SSS, not shown). The anomalous low salinity is much stronger in Spring 2014 compared to other years, even affecting the AW salinity in the basin interior. The effect of these fluctuations on the heat and salt content of LBE is discussed further in section 4.

4. Lofoten Basin Eddy Observations

4.1. An Example Transect

Figure 3 shows an example of a cross-basin section, from mission M2, including ESTs in the central basin between 69°N–70°N and 1°E–5°E. Warm and salty AW typically occupies the upper 500–700 m with temperatures exceeding 3°C, and with relatively warmer waters on the eastern part of the transect. As the glider samples through LBE in the central part of the basin, DAC exhibits large values with a mean speed of 0.5 m s^{-1} (maximum 0.8 m s^{-1}), and the Conservative Temperature (Θ) and Absolute Salinity (S_A) are quasi-uniform from surface to 1000 m, with average values of 4.75°C and 35.15 g kg^{-1}, respectively. The 29.7 isopycnal (representative of the lower boundary of AW) plummets inside the eddy. LBE thus forms a deep, voluminous heat and salt reservoir. The AW layer within LBE exceeds 1000 m. This transect is representative of the other crossings of the basin.

4.2. Radial Structure of LBE

Before presenting the detailed radial sections for each LBE realization, we exemplify the data coverage and DAC values from e7. Figure 4 shows the distribution of total DAC and $\overline{v_g}(r)$ with respect to the radial distance, as well as the depth-average vorticity. Typically, there are more than 10 dives in each 2 km radial bin out to two LBE radii. As expected, DAC amplitude is greater than its geostrophic component, by approximately 20% (with average values of -0.39 and -0.32 m s^{-1}, respectively) and is the largest at a distance of 15–20 km from the detected eddy center. The geostrophic DAC vorticity almost reaches the $-f/4$ limit within the eddy core (i.e., $4\overline{v_g}/rf$ approaches -1; cf. equation (2)). Using shipborne measurements of currents, *Søiland et al.* [2016] described a solid-body rotation of 7–8 km of the core with vorticity of $-f$. In agreement with this, Figure 4c shows a solid-body rotation extending to about 5 km from the center. Values of vorticity averaged within 5 km of the core (Table 3) reach as low as $-0.91f$, very close to the limit prescribed by the inertial instability limit for barotropic vortices [*Kloosterziel et al.*, 2007; *Lazar et al.*, 2013]. Vorticity rapidly approaches zero after the velocity maximum; in the example shown in Figure 4, the vorticity drops below 10% of its peak value at 22 km, only 6 km from the velocity maximum. This is comparable to where the relative vorticity of an isolated Gaussian vortex changes sign, i.e., $\sqrt{2}R$ [*Bosse et al.*, 2017]. In LBE, instead of becoming positive, the vorticity stays around zero toward the background, and the velocity decreases less rapidly.

Figure 5 shows the radial distribution of Θ and S_A of eight ESTs from e1 to e8. The deep water close to the LBE core (within 10 km) is warm and salty, with the mean Θ and S_A exceeding 4.6°C and 35.34 g kg^{-1}, respectively. While the core temperature and salinity in the deeper part of the water column is rather stable

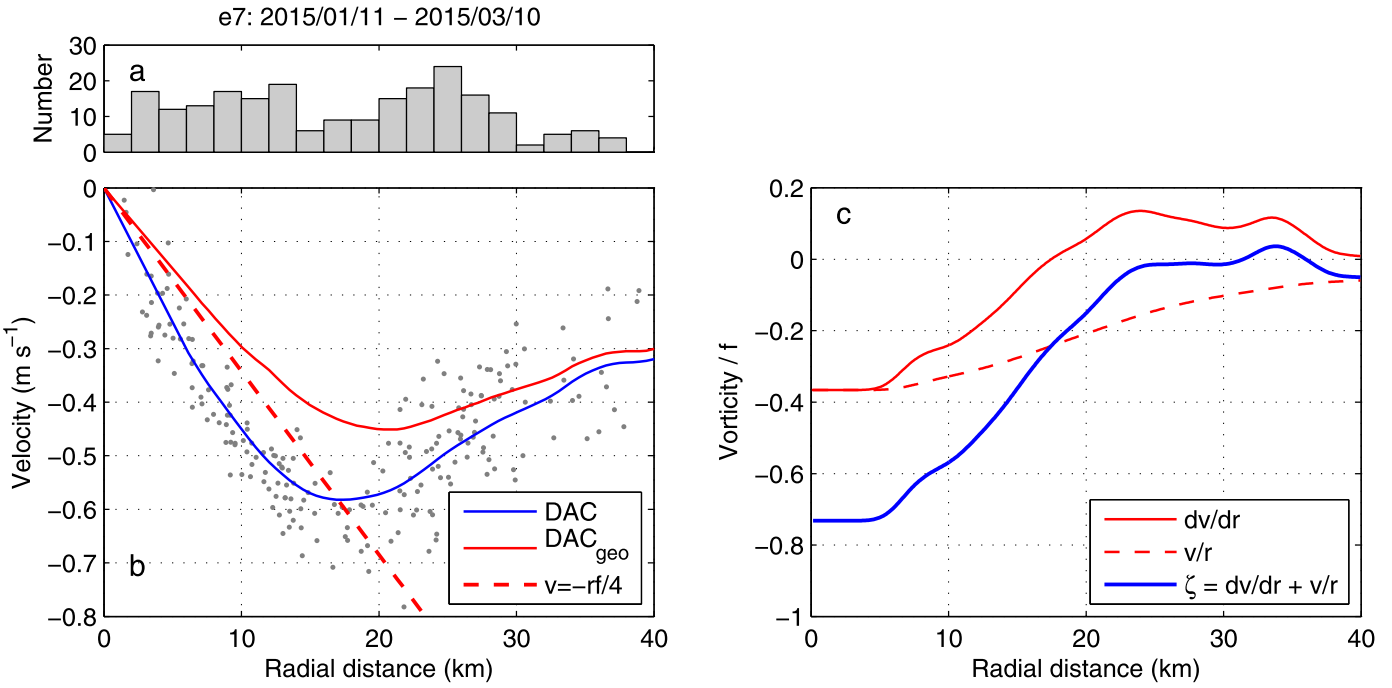

Figure 4. (a) The number of profiles in 2 km radial distance bins collected when sampling e7. (b) The radial distribution of 2 km bin-averaged (blue) total depth-average currents, DAC, and (red) its geostrophic component, DAC_{geo}, together with a red dashed line showing a slope of –f/4. Individual DAC values are shown in gray. (c) Vorticity structure from DAC, normalized by local Coriolis parameter, *f*.

in time, the values in the surface layer are highly variable, especially those of salinity. Note the presence of a 50 m thick layer of salinity in summer 2014 reaching values as low as 35.2 g kg^{-1} (Figure 5l), the surface layer gets clearly fresher by the end of the study period.

The maximum velocity is observed well below the surface, at depths between 700 and 900 m, and at a radial distance of 14–24 km from the eddy center. This corresponds to the buoyancy equilibrium depth, where the eddy buoyancy anomaly relative to the background vanishes. Heavier fluid is above the equilibrium depth (and lighter fluid is below). It is important to note that while the surface layers are becoming fresher and lighter, deeper isopycnals are progressively pushed down. For instance, the 27.85 kg m^{-3} isopycnal is depressed from about 500 m depth in 2013 to deeper than 1000 m 3 years later. The mean orbital

Table 3. Seaglider-Inferred Eddy Properties[a] and Comparison to Satellite Measurements[b] for Eddy Realizations e1–e8

Eddy	v_{cmax} (m s^{-1})	$r_{max} = R$ (km)	z_{max} (m)	$(v_c - v_g)/v_c$ (%)	N/f	B_u	R_{sat} (km)	ω/f ($\times 10^{-1}$)	ζ/f (<5 km)	Ro
e1	−0.63	20	767	34	21 ± 2.5	1.6 ± 0.6	36 ± 2	−0.88 ± 0.15	−0.63 ± 0.01	−0.49 ± 0.13
e2	−0.69	16	826	47	22 ± 2.3	2.7 ± 0.9	41 ± 2	−0.88 ± 0.15	−0.83 ± 0.00	−0.69 ± 0.14
e3	−0.56	24	689	45	14 ± 1.5	0.5 ± 0.2	38 ± 4	−0.73 ± 0.07	−0.77 ± 0.00	−0.44 ± 0.22
e4	−0.52	14	843	45	23 ± 0.7	3.9 ± 1.4	38 ± 3	−0.66 ± 0.15	−0.74 ± 0.04	−0.60 ± 0.18
e5	−0.61	15	850	48	24 ± 0.6	3.7 ± 1.3	38 ± 1	−0.88 ± 0.07	−0.89 ± 0.00	−0.68 ± 0.23
e6	−0.66	20	761	47	23 ± 0.6	1.9 ± 0.7	38 ± 4	−0.88 ± 0.15	−0.88 ± 0.00	−0.59 ± 0.25
e7	−0.71	16	857	47	23 ± 1.4	3.0 ± 1.0	40 ± 4	−0.80 ± 0.15	−0.88 ± 0.00	−0.71 ± 0.19
e8	−0.73	14	908	47	24 ± 1.0	4.2 ± 1.5	41 ± 3	−0.95 ± 0.15	−0.91 ± 0.00	−0.80 ± 0.15

[a] v_{cmax} is the cyclogeostrophic velocity maximum; r_{max} and z_{max} are the radial distance and depth where the cyclogeostrophic velocity reaches its maximum; the eddy radius *R* is equivalent to r_{max}. $(v_c\text{-}v_g)/v_c$ is the contribution of geostrophy in the cyclogeostrophic balance. *N/f* is averaged (±1 standard deviation) within a 100 m window centered at the depth of the LBE core 40–45 km far away from the LBE center. $B_u = (NH/fR)^2$ is the Burger number. Error estimate is obtained by propagating a 10% error in *N/f*, *H*, and *R*, assuming independent random error. ζ/f is core vorticity in solid-body rotation within the first 5 km. Ro = ζ_R/f is the Rossby number, where ζ_R is the vorticity averaged out to the position of the velocity maximum.

[b] R_{sat} and ω/f are the eddy radius and relative vorticity (ω normalized by the Coriolis parameter; compare to Ro) from satellite observations. Error estimate is ±1 standard deviation over values obtained for the duration of each eddy realization.

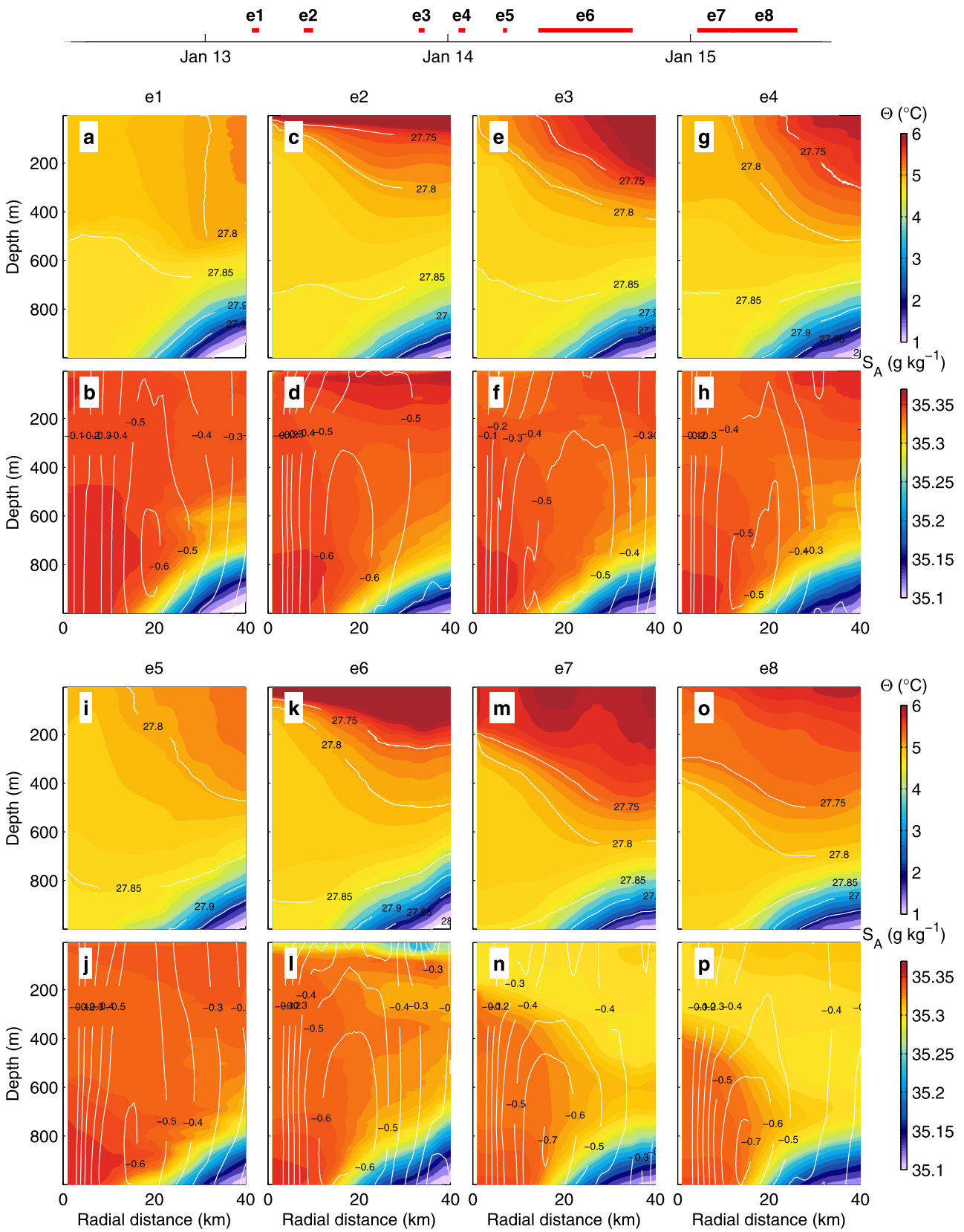

Figure 5. (continued)

velocity is 0.64 m s^{-1}, with the largest speed of 0.73 m s^{-1}. The minimum in vorticity is found near the eddy axis and reaches large negative values (–0.7 to $-0.91f$) very close to $-f$ (see also e7, Figure 4).

4.3. Rossby Number, Deformation Radius, and Burger Number

Eddy properties for each realization of LBE are listed in Table 3. The eddy radius, R, from the Seaglider observations is defined as the radial distance from the core to where the orbital velocity reaches its maximum. The mean eddy radius is 18 ($\pm$4) km, where the standard deviation is over the eight realizations of the eddy. Note that the orbital velocities decrease slowly outside the eddy, to 20–30 cm s^{-1} at 40 km (Figure 5). LBE thus influences a horizontal extent of over at least two radii from its center, but has a very confined core of high vorticity. The Rossby number here is computed from $\mathrm{Ro}=\zeta_R/f$, where ζ_R is the vorticity averaged from the eddy center to the eddy radius R, where the cyclogeostrophic velocity is maximum. The values of Ro range between -0.4 and -0.8 and emphasize the nonlinearity of this eddy. The average percentage accounted for by geostrophy in the cyclogeostrophic balance is 44%, which indicates the importance of the nongeostrophic effects. More detailed information can be found in Table 3.

The deformation radius $R_d=NH/f$, where H is the vertical extension of the eddy, is representative of the horizontal scale of oceanic eddies. Here H is defined as depth of the base of the eddy core, estimated as 1200 m using the full-depth CTD casts from *Søiland et al.* [2016] (the Seaglider data cover only the upper 1000 m). Figure 6 shows the radial stratification at e2. Close to the eddy center, the stratification is 10-fold weaker with N/f of 2 ($\pm$0.2) than in the surroundings where N/f reaches 22($\pm$2.3). The average and $\pm$1 standard deviation values are computed over a 100 m vertical range centered at the equilibrium depth of the eddy core. The Burger number, $\mathrm{Bu}=(NH/fR)^2=(R_d/R)^2$, can thus be computed and quantifies the ratio of the deformation radius to the eddy radius. Using N outside the eddy (40–45 km) and at its equilibrium depth, and the radius of 16 km for e2, we obtain $\mathrm{Bu}=2.7\pm0.9$. The error is estimated by propagating independent random errors of 10% in H, R, and N/f. The stratification and Burger number of seven other ESTs can be found in Table 3. The average Burger number is 2.7 ± 1.0, indicating that the LBE radius is comparable to the deformation radius. This result is in agreement with other estimates of Burger number observed for the subthermocline anticyclonic eddies [*D'Asaro*, 1988; *Timmermans et al.*, 2008; *Bower et al.*, 2013; *Pelland et al.*, 2013; *Bosse et al.*, 2015, 2016]. Note however that the length-scale convention used in the definition of Bu is not universal (e.g., *D'Asaro* [1988] uses diameter instead of radius).

4.4. Structure and Evolution of the LBE Core

The radial section of stratification shown for e2 (Figure 6) is typical for LBE. It shows that the deep stratified thermocline below AW at the periphery of LBE deepens from 700 m to the base of the eddy (typically at around 1200 m [*Søiland et al.*, 2016], not resolved with the glider observations). A complex vertical structure with a distinct intermediate thermocline is observed.

Time evolution of the weakly stratified layers observed within 5 km of the eddy center, reveals the formation of a new core layer each winter from 2013 to 2015 (Figure 7). Using the density profiles, quasi-uniform vertical layers are identified, and their average Θ and S_A are obtained. In total, four such core layers are detected (marked in Figure 7a). As time progresses, the cores deepen and temperature and salinity properties change; however, cores can still be tracked with their distinct Θ/S_A clustering (Figure 8). The evolution of each core in time is marked by letters a, b, c, and so on in Figure 7a, and color shading varies from dark (early) to bright (later after formation). A newly formed layer usually replaces the one from the previous winter. The deepest part of the eddy, however, is not affected by deep vertical mixing for the whole study period and can be identified as the core formed in winter 2012 [*Søiland et al.*, 2016]. The surface contact of the deep core in 2013 was not sampled with our data set, but its evolution and deepening can be followed by 1a–1e (Figure 7). In winter 2013, the mixing stopped at approximately 600 m and formed the core dubbed 2, by entraining the properties from the prevailing deep core. Then a new core (dubbed 3) with fresher and warmer characteristics completely replaces core 2 in winter 2014. The warming and freshening trend of the upper core is comparable for these two winter events: $+0.15$°C and -0.01 g kg^{-1}. Finally, in

Figure 5. Radial distance versus depth distributions of Conservative Temperature, Θ, and Absolute Salinity, S_A, for eddy realizations e1–e8. For each eddy set, upper panel shows Θ and the lower panel shows S_A. The white contours are drawn for potential density at 0.05 kg m^{-3} intervals on temperature panels, and for cyclogeostrophic velocity at 0.1 m s^{-1} intervals on the salinity panels. The occupation times of Eddy Samplings Tracks (ESTs) from e1 to e8 are marked on the time axis in the uppermost panel. For these sections data are gridded at 0.5 km radial bins and 1 m vertical bins, and smoothed over 10 km and 20 m.

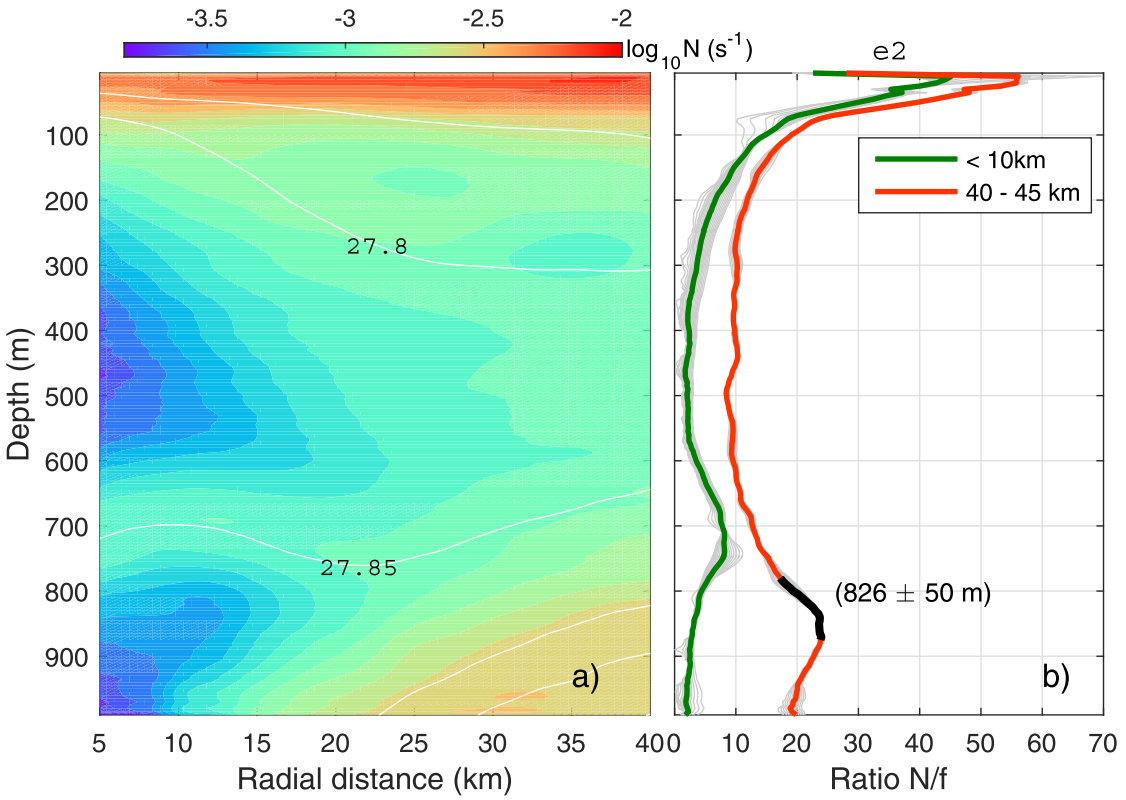

Figure 6. (a) Radial distribution of buoyancy frequency, *N* (in 10-base logarithm) for e2 with white contours showing the potential density at 0.05 kg m^{-3} intervals. (b) Profiles of stratification (buoyancy frequency normalized by the Coriolis parameter, *N/f*) near the eddy core ($r < 10$ km) and near the eddy periphery ($40 < r < 45$ km). Single profiles are shown in gray, and the average profiles are in green and red for the eddy core and periphery, respectively. The equivalent depth of the eddy core (826 m) and a ±50 m range over which *N/f* was averaged is marked in black.

winter 2015, convection did not even reach the base of this 600 m thick core from 2014 and formed a less saline (–0.03 g kg^{-1}) and warmer (+0.4°C) upper layer (core 4), green shades in Figures 7 and 8. This abrupt change can be partly attributed to vertical mixing that penetrated shallower, implying weaker entrainment at the base of the mixed layer. A major obstacle to vertical mixing was the strong near-surface layer stratification with the appearance of fresh water at the surface. This is also manifested in the observed change in the AW characteristics in summer 2014. In the past, the presence of a large pool of cold and fresh intermediate layer was reported to inhibit deep-reaching convection in the Irminger Sea in the 1990s [*Våge et al.*, 2011]. The origin and consequence of the freshening observed in LBE needs to be further investigated and is beyond the scope of this study.

It is worth noting that the deep core 1 (magenta shades) disappears from the resolved part of the water column (upper 1000 m) in 2014. This is not related to the vertical extent of convection and might be a result of the change of buoyancy anomaly of the upper part of the eddy. Deepening isopycnals (Figure 5) could be the result of an increase in the buoyancy anomaly related to the appearance of lighter waters in the upper part of the eddy. The equilibrium depth of deep cores can be affected by changes in the eddy buoyancy anomaly in the upper part of the eddy, which is influenced by a combination of freshwater input (such as the appearance of a fresh layer, as reported here) and winter mixing. There could also be fine-scale turbulence driving vertical and/or lateral exchanges between the core and the rim of eddy, but quantifying this aspect requires ocean microstructure profiles.

4.5. Heat and Salt Content Anomaly

Anomalies of heat and salt content (HC_a, SC_a) associated with LBE are computed using the gridded radial sections of each LBE realization (Figure 5) and assuming a radially symmetric eddy, as described in section 2.1.5. Figure 9 shows the heat and salt content anomaly of the core and of the rim of LBE. It is important to stress while HC_a and SC_a have approximately similar values when averaged within the LBE core or rim (e.g.,

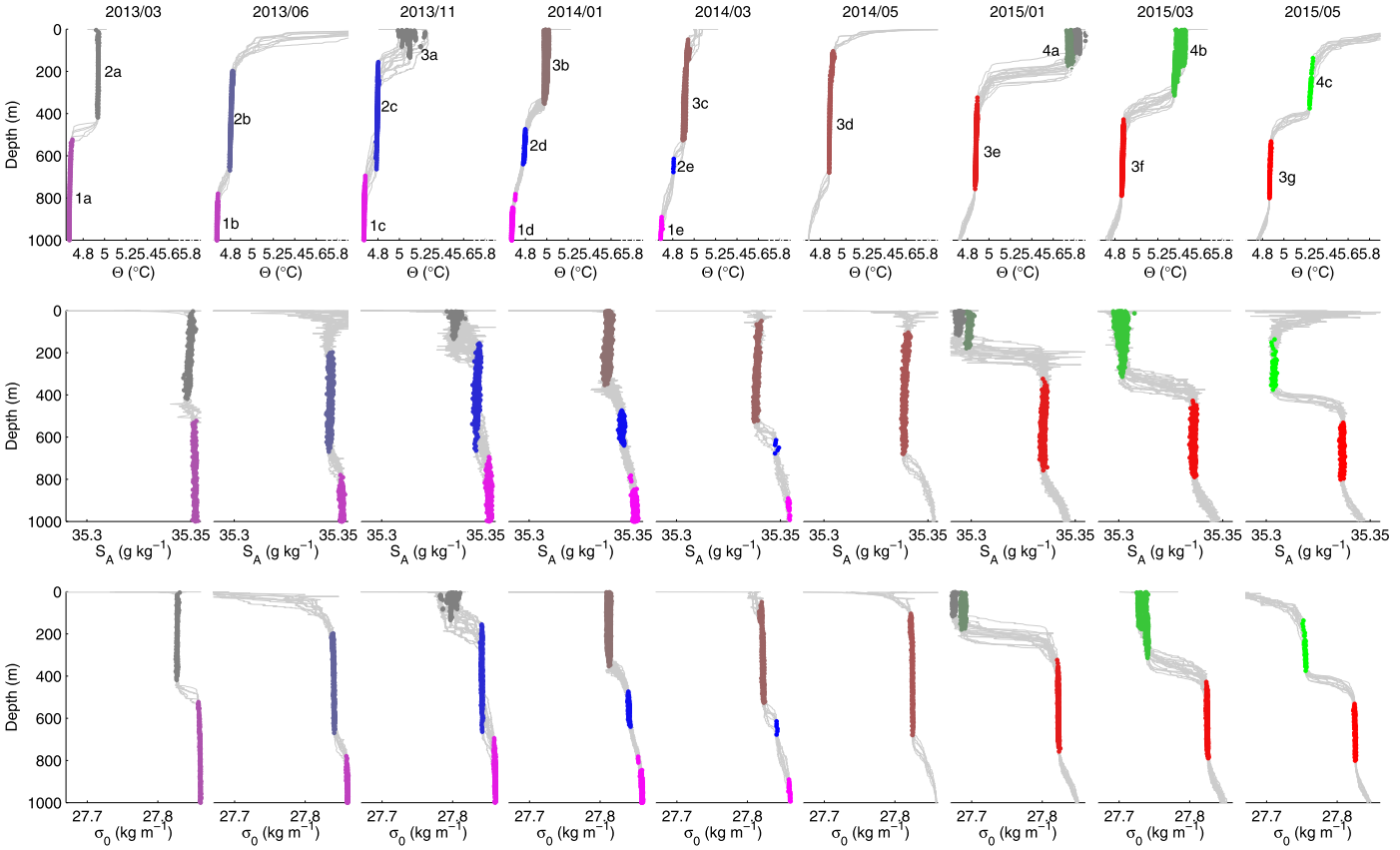

Figure 7. Water mass properties of the LBE core: Conservative Temperature, Θ (upper row), Absolute Salinity, S_A (middle row) and potential density, σ_θ (lowest row) sampled within 5 km to the center of LBE. The weakly stratified parts of the profiles are identified where $N/f < 3$ and colored according to a Θ-S_A identification of the cores (similar color represents the same core). In total, four cores are marked (1–4), with letters a, b, and so on for each core's evolution. The color is shaded with time (darker shades early in time) and use the same color scale as in Figure 8 with gray color corresponding to the first detection when the layer was in contact with the atmosphere.

HC_a is 1.1×10^{18} and 1.2×10^{18} J, respectively), the rim region has a much larger volume. The heat content anomaly per volume is thus smaller in the rim, as temperature values do not deviate largely from the background (an analogous statement can be made for the salt content anomaly). Figures 9b and 9e show the content anomalies divided by the corresponding volume of the rim and core regions. Magnitude and variability of the heat and salt content in the rim region could be indicative of the contribution from merging eddies shed from instability of the slope current.

An interesting feature is that prior to the freshening event reported in 2014, the heat and salt content of the rim is larger than that of the core. Following the freshening, the pattern is reversed, i.e., core has larger heat and salt content anomaly after 2014. This indicates that advection and lateral and vertical mixing might have been very effective in removing a large part of the heat and salt content from the rim into the core. Note that the deepest part of the core region between 1000 and 1200 m is not sampled, which leads to an underestimation of its heat and salt content by approximately 20%. While the observed evolution is robust, the absolute value of HC_a and SC_a within the core should be interpreted with caution.

The variability (manifested by the large error bars) is large, however, we note a general decrease in the heat and salt content anomaly per unit volume (about 0.01 kg m^{-3} and 2×10^8 J m^{-3} over 3 years) which suggests that the eddy signature is substantially affected by the changes in hydrographical conditions of the basin. The background profile shows indeed an interesting evolution characterized by stable HC, but a significant SC decrease of 0.04 ± 0.04 kg m^{-3} (see Figures 9c and 9f), about four times larger than that of the rim of LBE. The observation that the LBE rim follows the general trend in the basin, but with a smaller amplitude, suggests that the rim acts like a buffer zone for merging of eddies that transport anomalously low-salinity water from the slope toward the basin and eventually into LBE.

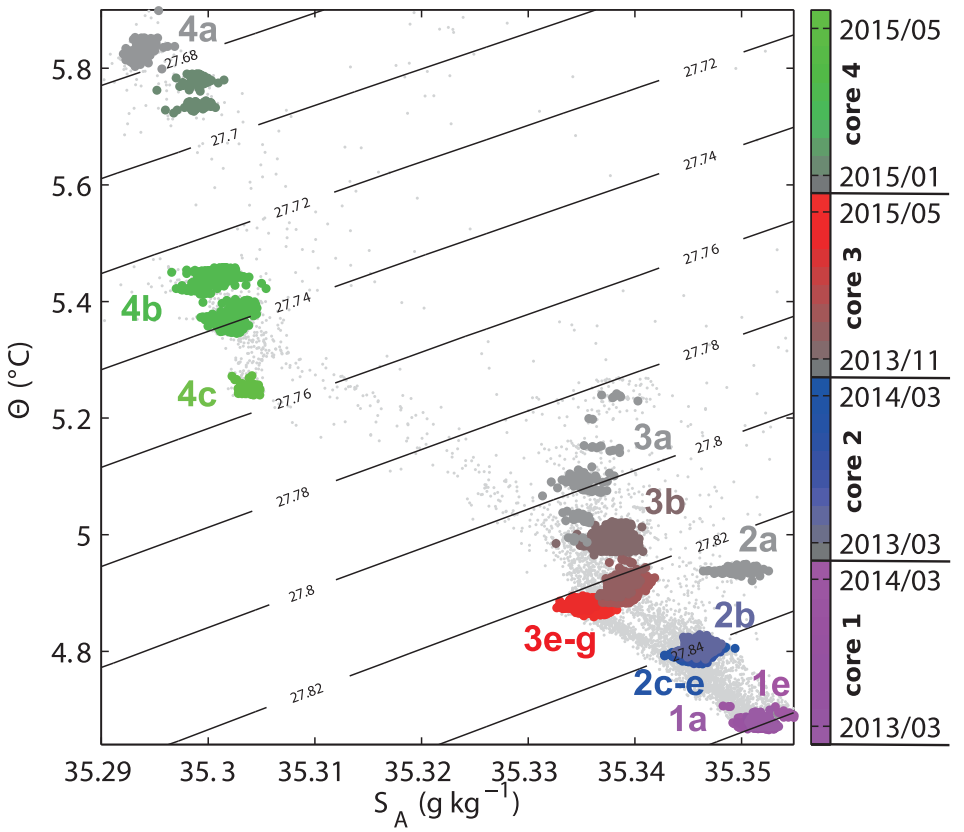

Figure 8. Θ-S_A diagram of the core profiles collected within 5 km to the LBE center. Slanted contours are for σ_θ. The four distinct weakly stratified cores identified in Figure 7 are plotted with color scale in time. Selected core clusters are labeled following Figure 7. Emphasized gray markers correspond to the first detection when the core was in contact with the atmosphere (not measured for core 1, March 2013).

4.6. Comparison With Eddy Properties Inferred From Satellite Altimetry

Several of the earlier studies that concentrated on LBE and the mesoscale energetics in LB were based on satellite altimeter data [e.g., *Raj et al*., 2015, 2016]. In these studies, the eddy parameters such as location, radius, relative vorticity, and kinetic energy inferred from the satellite observations were not evaluated against in situ observations, and their accuracy is uncertain. The glider data set offers a unique opportunity to evaluate the accuracy of remote sensing observations. The eddy center position is obtained independently from SSH measured by satellite, and from DAC measured by gliders. Figure 10 shows that the eddy position is detected satisfactorily by the satellite observations. For the e6 in the mission M4, the difference between two eddy center trajectories is small, with an average discrepancy of 7 km. Over all eddy realizations, the average difference is 8.5 km. Relative to the Seaglider measurements, the error in eddy position measured by satellite is approximately half the eddy radius defined from peak velocities, and is small compared to the overall extension of the eddy, which is typically larger than two radii. This accuracy is quite satisfactory. It is worth mentioning that in recent missions (not reported here), we successfully used remote sensing products to guide the gliders toward the LBE center.

For this anticyclonic LBE, the satellite based method using the geostrophic balance without taking account of the nonlinear effects is expected to underestimate the peak azimuthal velocity [*Elliott and Sanford*, 1986]. Furthermore, gridding and optimal interpolation methods used to produce SSH maps will lead to an overestimation of the eddy radius (Table 3). This leads to a much smaller vorticity and Rossby number inferred from the altimeter products. The LBE radii inferred from satellite vary between 30 and 50 km with a mean value of 40 km, i.e., about a factor of 2 larger than the value computed from glider observations (18 ± 4 km).

The eddy center trajectories from both methods (satellite and glider) are used to calculate eddy translation speeds. Figure 11 shows the trajectories and the calculated eddy propagation velocity for all LBE realizations

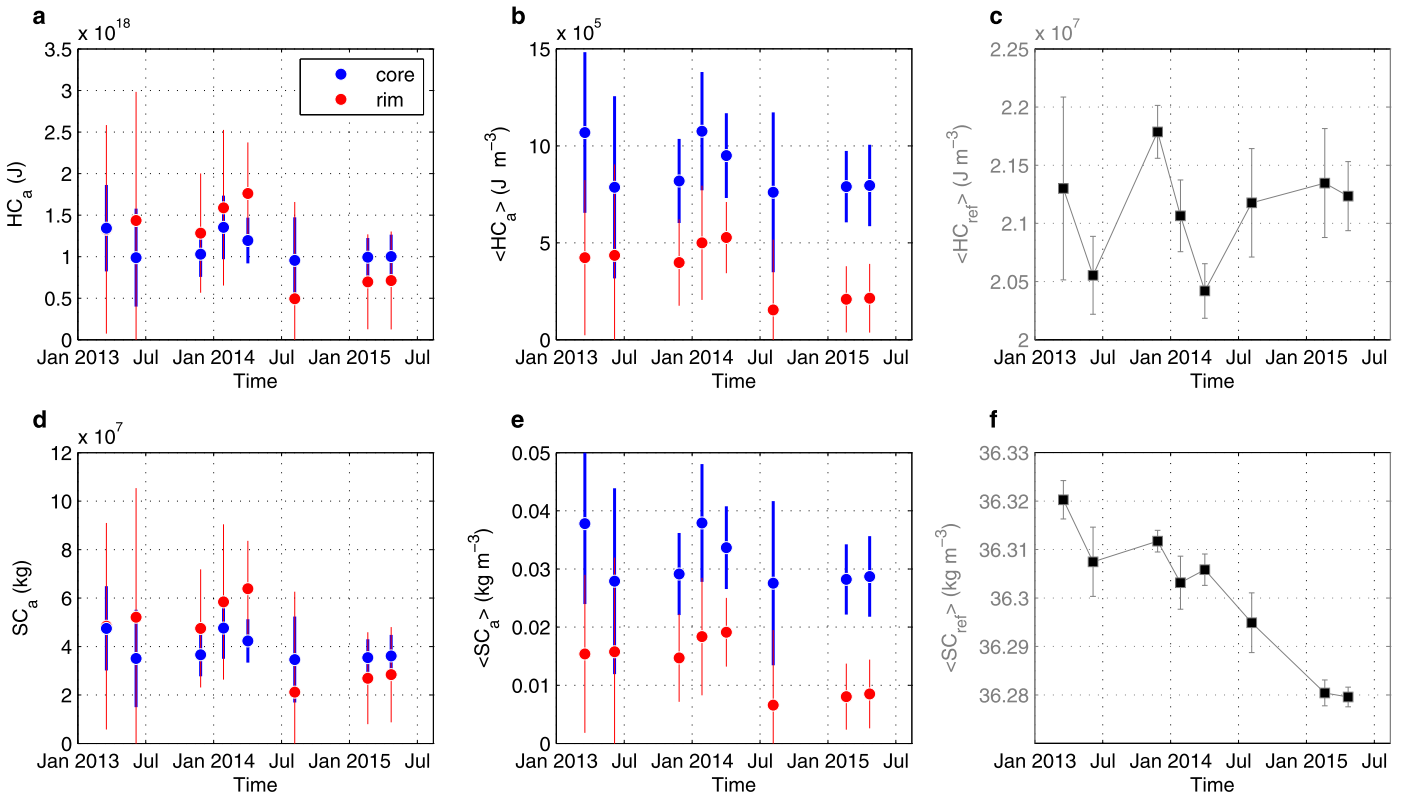

Figure 9. Time evolution of the (a) heat and (d) salt content anomaly of the LBE core ($0 < r < 20$ km) and rim ($20 < r < 40$ km) relative to the background hydrography in the area defined in Figure 1. Figures 9b and 9e show the anomaly per unit volume. Figures 9c and 9f show the heat and salt evolution of the background. Data points are obtained after integrating the temperature and salinity anomalies along isopycnals, whereas error bars are after integrating the ± one standard deviation of temperature and salinity anomalies along isopycnals.

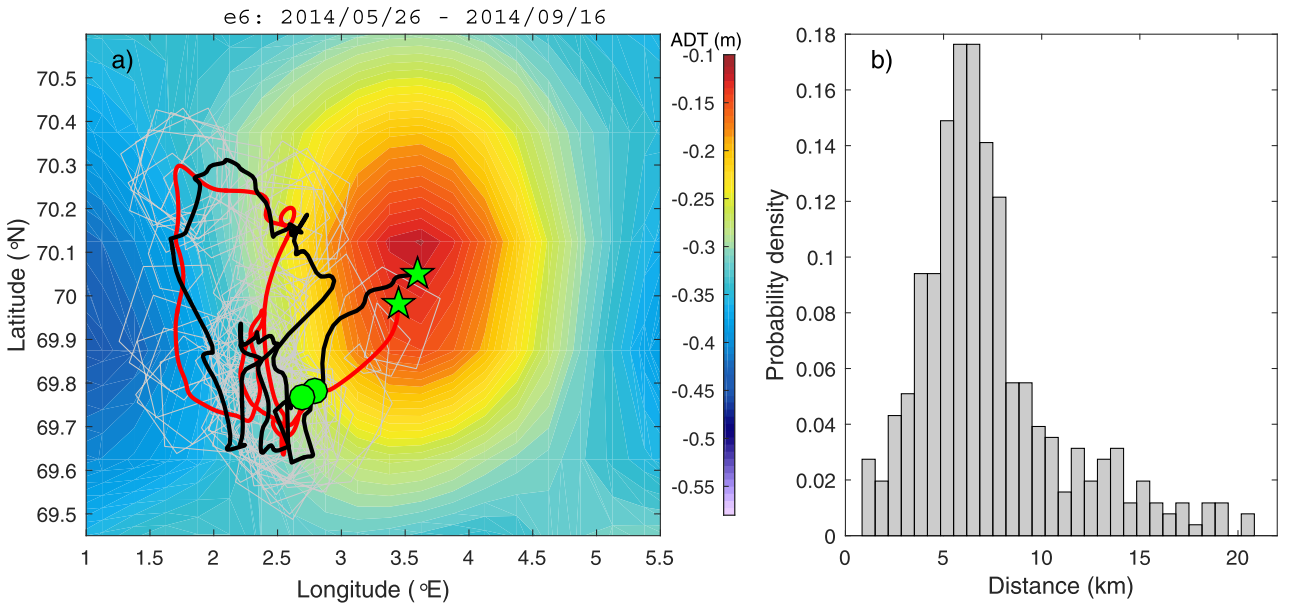

Figure 10. Comparison of the LBE center detection using Seaglider and satellite altimetry data for the eddy realization e6. (a) Eddy center trajectory from (red) glider and (black) altimetry. Background color is the ADT field at the start of e6, and the gray line shows the glider track spiraling around the time-varying eddy center location. Green stars and dots show the start and end point of the eddy center trajectory. (b) Histogram of horizontal distance between the glider and satellite detected eddy center location.

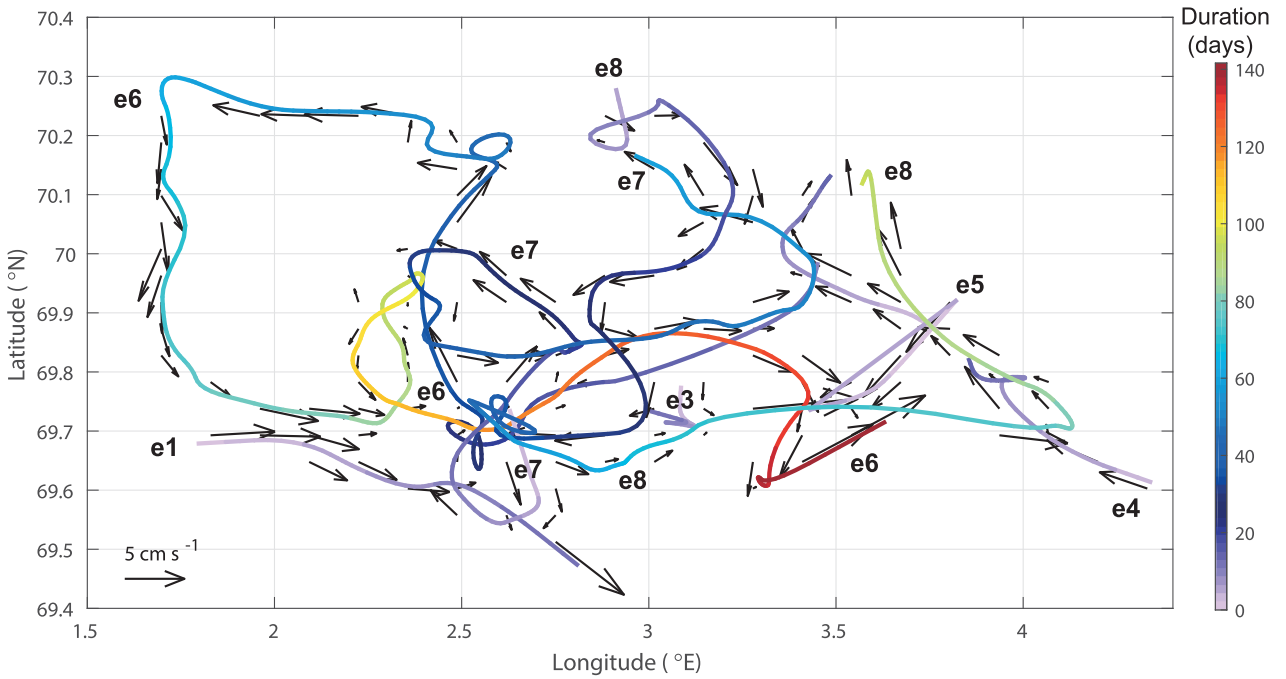

Figure 11. The propagation of the LBE center detected using glider data for all eight LBE realizations, indicated by e1–e8. The arrows represent the LBE translation velocity inferred from rate of change of the center position, and averaged in 10 km square bins. All eight tracks of the eddy centers are colored by their duration based on the start date of each realization.

sampled by Seagliders. Both Seaglider and satellite data sets show an apparent cyclonic translation of LBE, especially during the long period of ESTs from January 2015 to July 2015 (e7 and e8). The averaged drift speed from satellite observation is 4.3 cm s^{-1}, in agreement with that from gliders (3.4 cm s^{-1}), and both are similar to the eddy propagation speeds reported in *Volkov et al.* [2013] and *Raj et al.* [2015].

5. Discussion

5.1. Winter Mixing Preconditioning

The integrated wintertime buoyancy losses in the basin for the three observation years are 0.64, 0.57, and 0.64 m^2 s^{-2}, respectively. The prewinter stratification index, IS, during summer (6 May to 25 June 2013) in mission M2 (Figure 12) suggests that inside LBE, the convection in response to integrated buoyancy loss of winter 2014 exceeds 1000 m. In the surrounding region of the eddy, the vertical mixing is predicted to be much shallower with 593 ± 51 m. For the similar buoyancy loss around the eddy site, vertical mixing is inhibited by the stronger stratification of the deep pycnocline at the base of AW. This is consistent with the deepest MLDs of the basin observed within the eddy core (Figure 2c). Furthermore, the integrated buoyancy flux needed for the MLD to reach 500 m is about 3 times greater outside of the eddy than inside. This is mainly due to the shift in the deep thermocline at the base of AW. However, we have seen that the eddy and the basin gradually lose their salt content over the study period. When excess salt is present at intermediate depth, it can play an important role in the water column preconditioning to deep mixing [*Grignon et al.*, 2010]. The discrepancy between the actual integrated buoyancy loss in winter and the prewinter stratification index can be attributed to error in buoyancy fluxes from ERA Interim, the period of calculation (June–July, before winter begins), and the role of lateral advection of buoyancy, such as buoyant eddies shed from the shelf.

5.2. Comparison to the Labrador Sea, Greenland Sea, and Mediterranean Sea

LBE observations can be compared to other persistent deep subsurface eddies found in high latitudes (Greenland and Labrador Seas), as well as in the Mediterranean Sea.

Long-term evolution and dynamics of a long-lived warm core eddy in the Eastern Mediterranean Sea [*Brenner*, 1993] was related to winter mixing and relatively small changes in its position. Topography might play an important role in trapping such eddies within a certain area. While both eddies are affected by renewal

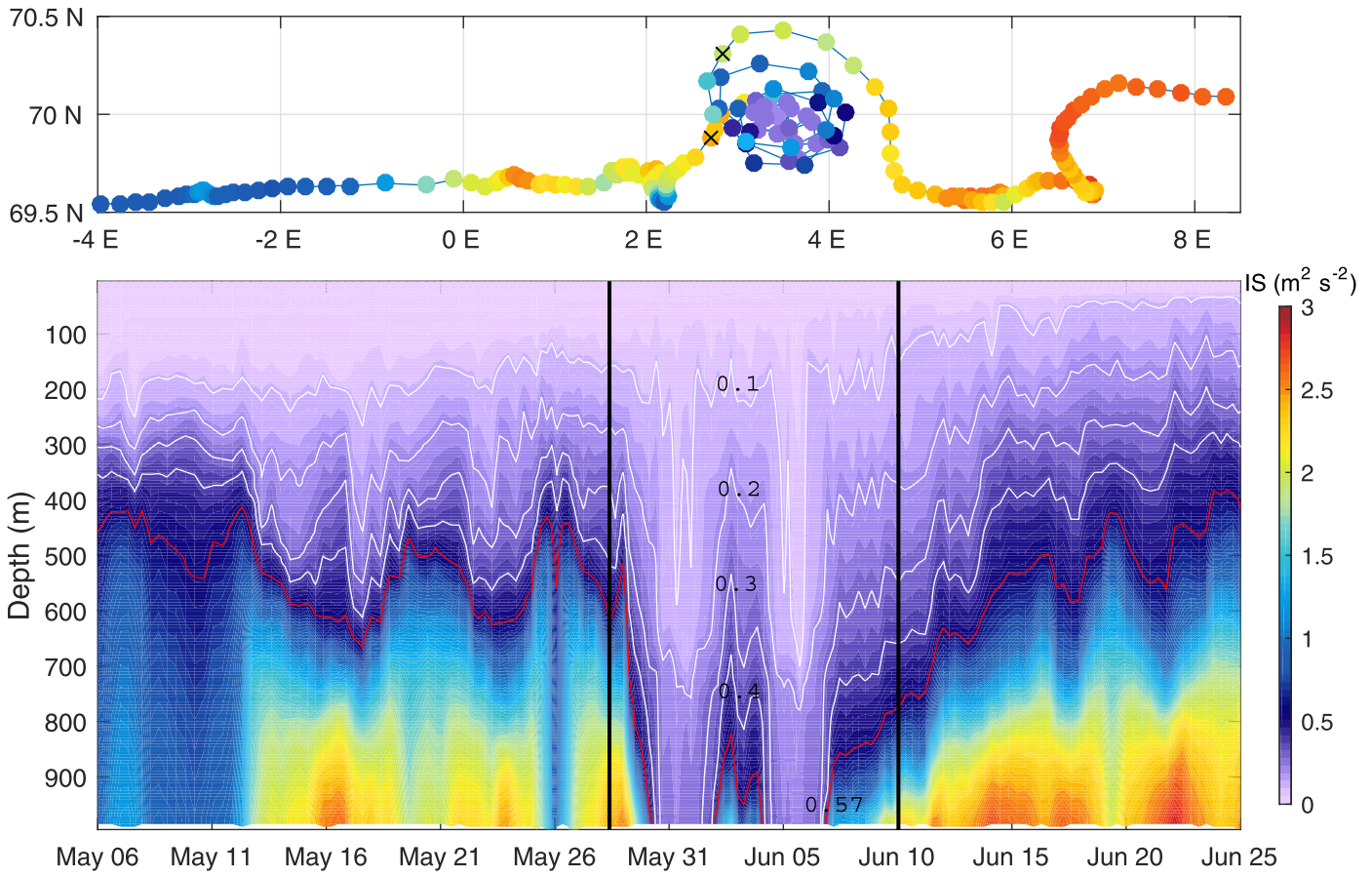

Figure 12. Columnar buoyancy, IS, section from the M2 mission (6 May to 25 June 2013) crossing LBE (between the black crosses and vertical lines). (top) Glider track from west to east together with the IS at 950 m. (bottom) IS along the track from surface to 1000 m, with selected contours in white and the IS = 0.57 m^2 s^{-2} contour in red.

or exchange of upper core water by winter convection, unlike LBE which is located in the deepest part of the basin, the warm core Cyprus eddy stays in the vicinity of a seamount located south of Cyprus.

Postconvective submesoscale vortices were found to play an important role in the dispersion of convected water in deep water formation regions in the Labrador Sea [*Lilly and Rhines*, 2002] and the northwestern Mediterranean Sea [*Testor and Gascard*, 2006; *Bosse et al.*, 2016]. They have many similarities to LBE, such as a deep velocity maximum, small radius and intense velocity (i.e., Rossby number near unity). A notable difference is that, in contrast to LBE, they move over long distances [*Lilly and Rhines*, 2002; *Testor and Gascard*, 2006; *Bower et al.*, 2013]. Their velocity distribution is also more confined and decreases rapidly toward the background field [*Bosse et al.*, 2017], whereas LBE is characterized by an important radial extension, reaching beyond its hydrological core. The periphery of LBE forms a buffer zone for interaction with other eddies. Similar to LB, the Labrador and the northwestern Mediterranean Seas experience significant wintertime destabilizing surface buoyancy fluxes, but the vertical mixing inside LBE is restricted to the AW layer in the upper 600–700 m. Some of the relevant dynamics common between the Labrador Sea and LB have been discussed in *Richards and Straneo* [2015]. Irminger Current Anticyclones (or Irminger Rings) play an important role in the advection of heat into the central Labrador Sea due to their anomalous warm cores, and are argued to account for between 25 and 100% of the heat needed to balance the surface heat loss during wintertime [*Lilly et al.*, 2003; *Katsman et al.*, 2004; *Hátún et al.*, 2007; *Rykova et al.*, 2009; *Fan et al.*, 2013]. Similar to Lofoten Eddies (see an example at 10°E, Figure 3) shed from the slope current [*Köhl*, 2007; *Raj et al.*, 2015, 2016; *Søiland et al.*, 2016], Irminger Rings are triggered from the west Greenland boundary current over steep topography [*Lilly et al.*, 2003; *Katsman et al.*, 2004; *Hátún et al.*, 2007; *Rykova et al.*, 2009].

Richards and Straneo [2015] show that despite lacking a cyclonic boundary current (compared to the Labrador Sea), the eddy-flux per unit length is larger in LB and leads to vigorous boundary-interior lateral

exchange that maintains a pool of warm water and substantial densification there. The vertical structure of LBE and its role on the deep layer ventilation can be compared to the long-lived (2–3 years) Greenland Sea coherent vortices described by *Budéus et al*. [2004] and *Ronski and Budéus* [2006]. Different from LBE, the vertical homogeneity in the Greenland Sea vortices is established mainly by vertical mixing in winter with negligible lateral exchange. Convective history in a vortex leads to multiple layers depending on the previous winter's forcing and hydrographic conditions of the surrounding waters. This is reminiscent of the layered structure we observe in the LBE core. LBE shows evidence of substantial interannual variability in water properties (Figures 7, 8 and 9), and is potentially influenced by surface buoyancy flux and advection of anomalous low-salinity near-surface waters that may affect the extent of winter convection. Conclusions about the interannual variability of LBE, and possible winter amplification through convective processes cannot be drawn given the limited duration of our observations.

6. Summary and Conclusions

A detailed description of the vertical and radial structure, evolution in time, and dynamical characteristics of the Lofoten Basin Eddy (LBE) is given using 3 years of Seaglider observations from July 2012 to July 2015. LBE has a mean radius of 18 ± 4 km and peak azimuthal velocity of 0.5–0.7 m s^{-1} located at the depths between 700 and 900. LBE is nonlinear and characterized by Rossby number varying between -0.4 and -0.8. Geostrophy accounts for 44% in the cyclogeostrophic balance. Vorticity near the core approaches $-f$, the theoretical limit for centrifugal instability for barotropic eddies. Burger number is 2.7 ± 1.0, on the average, indicating that the deformation radius is comparable to the LBE radius.

Using the Seaglider observations from eight realizations of LBE as a baseline, the accuracy of basic eddy characteristics (for LBE) obtained from standard, gridded satellite altimetry products is evaluated. The location of the eddy center is successfully inferred from satellite altimetry to within one half LBE radius. The accurate positioning of the eddy center also allows for reliable estimates of eddy translation track and velocity, which compare well with the glider data. Altimeter-based results, however, overestimate the radius and underestimate the vorticity by a factor of 2.

The time evolution of the weakly stratified layers observed within 5 km of the eddy center, reveals the formation of a new core layer each winter from 2013 to 2015. As time progresses, the cores deepen. The observation period experienced a freshening event in 2014, which likely played a role in inhibiting deep convection the following winter. Through the period of observations, the salt content of the background surroundings outside the eddy decreases significantly. The heat and salt content anomaly in the core compared to the background decreased less rapidly. This implies that the rim region, characterized by higher variability and more rapid reaction to changes in the basin, is a buffer zone for lateral exchange and interactions with other eddies. The interannual variability, effect of winter convection, the mechanisms of lateral and vertical mixing, role of eddy periphery, and interactions with eddies shed from the boundary current merit continued investigation for multiple years throughout the annual cycle. Persistent autonomous observations such as demonstrated here are feasible in winter and can yield detailed information.

Acknowledgments
The Seaglider observations in this study were provided by the Norwegian Atlantic Current Observatory (NACO), a national research infrastructure which has received funding from the Norwegian Research Council through contract 197316 with the Geophysical Institute, University of Bergen. The research is conducted during LY's visit at the University of Bergen, supported by the scholarship from the Joint PhD Training Program of the University of Chinese Academy of Sciences. L.Y. thanks Sheng-Qi Zhou for his guidance and fruitful discussions. A.B. and I.F. received funding from the Research Council of Norway, through the project "Watermass transformation processes and vortex dynamics in the Lofoten Basin of the Norwegian Sea" (PROVOLO), project number 250784. We would like to thank Bastien Queste for making the data processing software available and advice on data processing, Jim Bennett for advice on Seaglider technicalities, Peter M. Haugan for leadership in NACO, and Tor de Lange, Helge Bryhni, and Steinar Myking for technical assistance. Comments from Noel Pelland and an anonymous reviewer were very helpful in improving the manuscript. The CTD data managed by the Institute of Marine Research, Bergen, are available through the Norwegian Marine Data Center. The Seaglider data set is available from Copernicus CMEMS as a part of the product INSITU_ARC_NRT_OBSERVATIONS_013_031, and from the NACO glider web site at http://naco.gfi.uib.no/page/figs.html. ERA Interim reanalysis data are available at http://apps.ecmwf.int. The altimeter products were produced by Ssalto/Duacs and distributed by Aviso, with support from CNES.

References

Alexeev, G. V., M. V. Bagryantsev, P. V. Bogorodsky, V. B. Vasin, and P. E. Shirokov (1991), Structure and circulation of water masses in the area of an anticyclonic vortex in the north-eastern part of the Norwegian Sea [in Russian], in *Russian Problems of Arctic and Antarctic*, vol. 65, Gidrometeoizdat, Leningrad.

Andersson, M., K. A. Orvik, J. H. LaCasce, I. Koszalka, and C. Mauritzen (2011), Variability of the Norwegian Atlantic Current and associated eddy field from surface drifters, *J. Geophys. Res.*, *116*, C08032, doi:10.1029/2011JC007078.

Bosse, A., P. Testor, L. Mortier, L. Prieur, V. Taillandier, F. d'Ortenzio, and L. Coppola (2015), Spreading of Levantine Intermediate Waters by submesoscale coherent vortices in the northwestern Mediterranean Sea as observed with gliders, *J. Geophys. Res.*, *120*, 1599–1622, doi:10.1002/2014JC010263.

Bosse, A., et al. (2016), Scales and dynamics of submesoscale coherent vortices formed by deep convection in the northwestern Mediterranean Sea, *J. Geophys. Res.*, *121*, 7716–7742, doi:10.1002/2016JC012144.

Bosse, A., P. Testor, N. Mayot, L. Prieur, F. D'Ortenzio, L. Mortier, H. Le Goff, C. Gourcuff, L. Coppola, H. Lavigne, and P. Raimbault (2017), A submesoscale coherent vortex in the Ligurian Sea: From dynamical barriers to biological implications, *J. Geophys. Res. Oceans*, *122*, doi:10.1002/2016JC012634.

Bower, A. S., R. M. Hendry, D. E. Amrhein, and J. M. Lilly (2013), Direct observations of formation and propagation of subpolar eddies into the Subtropical North Atlantic, *Deep Sea Res., Part II*, *85*, 15–41, doi:10.1016/j.dsr2.2012.07.029.

Brenner, S. (1993), Long-term evolution and dynamics of a persistent warm core eddy in the Eastern Mediterranean Sea, *Deep Sea Res., Part II*, *40*, 1193–1206, doi:10.1016/0967-0645(93)90067-W.

Budéus, G., B. Cisewski, S. Ronski, D. Dietrich, and M. Weitere (2004), Structure and effects of a long lived vortex in the Greenland Sea, *Geophys. Res. Lett.*, *31*, L05304, doi:10.1029/2003GL017983.
Chelton, D. B., M. G. Schlax, R. M. Samelson, and R. A. de Szoeke (2007), Global observations of large oceanic eddies, *Geophys. Res. Lett.*, *34*, L15606, doi:10.1029/2007GL030812.
Chelton, D. B., M. G. Schlax, and R. M. Samelson (2011), Global observations of nonlinear mesoscale eddies, *Prog. Oceanogr.*, *91*, 167–216, doi:10.1016/j.pocean.2011.01.002.
D'Asaro, E. A. (1988), Observations of small eddies in the Beaufort Sea, *J. Geophys. Res.*, *93*, 6669–6684, doi:10.1029/JC093iC06p06669.
de Boyer Montégut, C., G. Madec, A. S. Fischer, A. Lazar, and D. Iudicone (2004), Mixed layer depth over the global ocean: An examination of profile data and a profile-based climatology, *J. Geophys. Res.*, *109*, C12003, doi:10.1029/2004JC002378.
Dee, D. P., et al. (2011), The ERA-Interim reanalysis: Configuration and performance of the data assimilation system, *Q. J. R. Meteorol. Soc.*, *137*, 553–597, doi:10.1002/qj.828.
Elliott, B. A., and T. B. Sanford (1986), The subthermocline Lens D1. Part II: Kinematics and dynamics, *J. Phys. Oceanogr.*, *16*, 549–561, doi:10.1175/1520-0485(1986)016<0549:tsldpi>2.0.co;2.
Eriksen, C. C., T. J. Osse, R. D. Light, T. Wen, T. W. Lehman, P. L. Sabin, J. W. Ballard, and A. M. Chiodi (2001), Seaglider: A long-range autonomous underwater vehicle for oceanographic research, *IEEE J. Oceanic Eng.*, *26*, 424–436, doi:10.1109/48.972073.
Fan, X., U. Send, P. Testor, J. Karstensen, and P. Lherminier (2013), Observations of Irminger Sea anticyclonic eddies, *J. Phys. Oceanogr.*, *43*, 805–823, doi:10.1175/JPO-D-11-0155.1.
Grignon, L., D. A. Smeed, H. L. Bryden, and K. Schroeder (2010), Importance of the variability of hydrographic preconditioning for deep convection in the Gulf of Lion, NW Mediterranean, *Ocean Sci.*, *6*, 573–586, doi:10.5194/os-6-573-2010.
Halo, I. (2012), The Mozambique Channel eddies: Characteristics and mechanisms of formation, PhD thesis. Univ. of Cape Town, Cape Town, South Africa.
Halo, I., B. Backeberg, P. Penven, I. Ansorge, C. Reason, and J. E. Ullgren (2014), Eddy properties in the Mozambique Channel: A comparison between observations and two numerical ocean circulation models, *Deep Sea Res., Part II*, *100*, 38–53, doi:10.1016/j.dsr2.2013.10.015.
Hátún, H., C. C. Eriksen, and P. B. Rhines (2007), Buoyant eddies entering the Labrador Sea observed with gliders and altimetry, *J. Phys. Oceanogr.*, *37*, 2838–2854, doi:10.1175/2007JPO3567.1.
IOC, SCOR, and IAPSO (2010), The international thermodynamic equation of seawater - 2010: Calculations and use of thermodynamic properties, in *Manuals and Guides*, vol. 56, Intergov. Oceanogr. Commiss., UNESCO, 196 pp.
Isern-Fontanet, J., E. García-Ladona, and J. Font (2006), Vortices of the Mediterranean Sea: An altimetric perspective, *J. Phys. Oceanogr.*, *36*, 87–103, doi:10.1175/jpo2826.1.
Ivanov, V., and A. A. Korablev (1995a), Dynamics of an intrapycnocline lens in the Norwegian Sea, *Russ. Meteor. Hydrol.*, *10*, 32–37.
Ivanov, V., and A. A. Korablev (1995b), Formation and regeneration of the pycnocline lens in the Norwegian Sea, *Russ. Meteor. Hydrol.*, *9*, 62–69.
Katsman, C. A., M. A. Spall, and R. S. Pickart (2004), Boundary Current eddies and their role in the restratification of the Labrador Sea, *J. Phys. Oceanogr.*, *34*, 1967–1983, doi:10.1175/1520-0485(2004)034<1967:bceatr>2.0.co;2.
Kloosterziel, R. C., G. F. Carnevale, and P. Orlandi (2007), Inertial instability in rotating and stratified fluids: Barotropic vortices, *J. Fluid Mech.*, *583*, 379–412, doi:10.1017/S0022112007006325.
Köhl, A. (2007), Generation and stability of a quasi-permanent vortex in the Lofoten Basin, *J. Phys. Oceanogr.*, *37*, 2637–2651, doi:10.1175/2007JPO3694.1.
Koszalka, I., J. H. LaCasce, M. Andersson, K. A. Orvik, and C. Mauritzen (2011), Surface circulation in the Nordic Seas from clustered drifters, *Deep Sea Res., Part I*, *58*, 468–485, doi:10.1016/j.dsr.2011.01.007.
Koszalka, I., J. H. LaCasce, and C. Mauritzen (2013), In pursuit of anomalies—Analyzing the poleward transport of Atlantic Water with surface drifters, *Deep Sea Res., Part II*, *85*, 96–108, doi:10.1016/j.dsr2.2012.07.035.
Lazar, A., A. Stegner, and E. Heifetz (2013), Inertial instability of intense stratified anticyclones. Part 1. Generalized stability criterion, *J. Fluid Mech.*, *732*, 457–484, doi:10.1017/jfm.2013.412.
Lilly, J. M., and P. B. Rhines (2002), Coherent eddies in the Labrador Sea observed from a mooring, *J. Phys. Oceanogr.*, *32*, 585–598, doi:10.1175/1520-0485(2002)032<0585:Ceitls>2.0.Co;2.
Lilly, J. M., P. B. Rhines, F. Schott, K. Lavender, J. Lazier, U. Send, and E. D'Asaro (2003), Observations of the Labrador Sea eddy field, *Prog. Oceanogr.*, *59*, 75–176, doi:10.1016/j.pocean.2003.08.013.
McWilliams, J. C. (2006), *Fundamentals of Geophysical Fluid Dynamics*, 249 pp., Cambridge Univ. Press, Cambridge, U. K.
Nilsen, J. E. O., and E. Falck (2006), Variations of mixed layer properties in the Norwegian Sea for the period 1948–1999, *Prog. Oceanogr.*, *70*, 58–90, doi:10.1016/j.pocean.2006.03.014.
Orvik, K. A., and P. Niiler (2002), Major pathways of Atlantic water in the northern North Atlantic and Nordic Seas toward Arctic, *Geophys. Res. Lett.*, *29*(19), 1896, doi:10.1029/2002GL015002.
Pelland, N. A., C. C. Eriksen, and C. M. Lee (2013), Subthermocline eddies over the Washington continental slope as observed by Seagliders, 2003–09, *J. Phys. Oceanogr.*, *43*, 2025–2053, doi:10.1175/JPO-D-12-086.1.
Poulain, P. M., A. Warn-Varnas, and P. P. Niiler (1996), Near-surface circulation of the Nordic seas as measured by Lagrangian drifters, *J. Geophys. Res.*, *101*, 18,237–18,258, doi:10.1029/96JC00506.
Raj, R. P., L. Chafik, J. E. Ø. Nilsen, T. Eldevik, and I. Halo (2015), The Lofoten vortex of the Nordic Seas, *Deep Sea Res., Part I*, *96*, 1–14, doi:10.1016/j.dsr.2014.10.011.
Raj, R. P., J. A. Johannessen, T. Eldevik, J. E. Ø. Nilsen, and I. Halo (2016), Quantifying mesoscale eddies in the Lofoten Basin, *J. Geophys. Res.*, *121*, 4503–4521, doi:10.1002/2016JC011637.
Richards, C. G., and F. Straneo (2015), Observations of water mass transformation and eddies in the Lofoten Basin of the Nordic Seas, *J. Phys. Oceanogr.*, *45*, 1735–1756, doi:10.1175/JPO-D-14-0238.1.
Ronski, S., and G. Budéus (2006), Vertical structure reveals eddy lifetime in the Greenland Sea, *Geophys. Res. Lett.*, *33*, L11602, doi:10.1029/2006GL026045.
Rossby, T., V. Ozhigin, V. Ivshin, and S. Bacon (2009a), An isopycnal view of the Nordic Seas hydrography with focus on properties of the Lofoten Basin, *Deep Sea Res., Part I*, *56*, 1955–1971, doi:10.1016/j.dsr.2009.07.005.
Rossby, T., M. D. Prater, and H. Søiland (2009b), Pathways of inflow and dispersion of warm waters in the Nordic seas, *J. Geophys. Res.*, *114*, C04011, doi:10.1029/2008JC005073.
Rudnick, D. L. (2016), Ocean research enabled by underwater gliders, *Annu. Rev. Mar. Sci.*, *8*, 519–541, doi:10.1146/annurev-marine-122414-033913.

Rykova, T., F. Straneo, J. M. Lilly, and I. Yashayaev (2009), Irminger Current anticyclones in the Labrador Sea observed in the hydrographic record, 1990–2004, *J. Mar. Res.*, *67*, 361–384, doi:10.1357/002224009789954739.

Søiland, H., and T. Rossby (2013), On the structure of the Lofoten Basin Eddy, *J. Geophys. Res.*, *118*, 4201–4212, doi:10.1002/jgrc.20301.

Søiland, H., L. Chafik, and T. Rossby (2016), On the long-term stability of the Lofoten Basin Eddy, *J. Geophys. Res. Oceans*, *121*, 4438–4449, doi:10.1002/2016JC011726.

Testor, P., and J. C. Gascard (2006), Post-convection spreading phase in the Northwestern Mediterranean Sea, *Deep Sea Res., Part I*, *53*, 869–893, doi:10.1016/j.dsr.2006.02.004.

Timmermans, M.-L., J. Toole, A. Proshutinsky, R. Krishfield, and A. Plueddemann (2008), Eddies in the Canada Basin, Arctic Ocean, observed from ice-tethered profilers, *J. Phys. Oceanogr.*, *38*, 133–145, doi:10.1175/2007jpo3782.1.

Voet, G., D. Quadfasel, K. A. Mork, and H. Søiland (2010), The mid-depth circulation of the Nordic Seas derived from profiling float observations, *Tellus, Ser. A*, *62*, 516–529, doi:10.1111/j.1600-0870.2010.00444.x.

Volkov, D. L., and M. I. Pujol (2012), Quality assessment of a satellite altimetry data product in the Nordic, Barents, and Kara seas, *J. Geophys. Res.*, *117*, C03025, doi:10.1029/2011JC007557.

Volkov, D. L., T. V. Belonenko, and V. R. Foux (2013), Puzzling over the dynamics of the Lofoten Basin—A sub-Arctic hot spot of ocean variability, *Geophys. Res. Lett.*, *40*, 738–743, doi:10.1002/grl.50126.

Volkov, D. L., A. A. Kubryakov, and R. Lumpkin (2015), Formation and variability of the Lofoten basin vortex in a high-resolution ocean model, *Deep Sea Res., Part I*, *105*, 142–157, doi:10.1016/j.dsr.2015.09.001.

Våge, K., R. S. Pickart, A. Sarafanov, Ø. Knutsen, H. Mercier, P. Lherminier, H. M. van Aken, J. Meincke, D. Quadfasel, and S. Bacon (2011), The Irminger Gyre: Circulation, convection, and interannual variability, *Deep Sea Res., Part I*, *58*, 590–614, doi:10.1016/j.dsr.2011.03.001.